

AN ABSTRACT OF THE THESIS OF

Stephen J. Redfield for the degree of Master of Science in
Electrical and Computer Engineering presented on June 4, 2010.

Title: Understanding the Ultra-wideband Channel within a Computer Chassis

Abstract approved: _____

Huaping Liu

Recent developments in computing technology have generated a demand for more streamlined and effective test systems. By replacing traditional in-chassis wired interconnects with a broadcast wireless system, fault detection and error susceptibility will drastically improve, input/output capabilities will expand, and routing complexity will decrease. Ultra-wideband impulse radio's (UWB-IR) characteristic multipath-immunity and free-licensed spectrum makes it ideal for use in this scenario. Understanding the unique and complex communications channel within the confines of a computer is vital to any future system implementation. A comprehensive measurement campaign is mounted with the goal of thoroughly characterizing this channel. A UWB channel model specifying channel impulse response (CIR), path loss, and fading characteristics is derived and presented in enough detail to be used as a guide for future channel modeling endeavors. Analysis of this model provides a baseline for a proof-of-concept

communications system consisting of a UWB pulser and receiver, which are implemented on printed circuit board (PCB) to decrease prototyping costs. These devices are then implemented within the channel of interest to find a UWB pulse response. The pulse response measurement is a simple experiment which takes into account the pulse distortion and delay spread shortening effects of UWB antennas and in-channel radiating interference, which are not apparent in the traditional channel model. The comprehensive model is then used to determine any issues that may arise during the conversion from wired to wireless interconnects among a computer's integrated circuits (IC).

© Copyright by Stephen J. Redfield
June 4, 2010
All Rights Reserved

Understanding the Ultra-wideband Channel within a Computer
Chassis

by

Stephen J. Redfield

A THESIS

submitted to

Oregon State University

in partial fulfillment of
the requirements for the
degree of

Master of Science

Presented June 4, 2010
Commencement June 2010

Master of Science thesis of Stephen J. Redfield presented on June 4, 2010.

APPROVED:

Major Professor, representing Electrical and Computer Engineering

Director of the School of Electrical Engineering and Computer Science

Dean of the Graduate School

I understand that my thesis will become part of the permanent collection of Oregon State University libraries. My signature below authorizes release of my thesis to any reader upon request.

Stephen J. Redfield, Author

ACKNOWLEDGEMENTS

First I would like to acknowledge my advising professor Dr. Huaping Liu. From advising my undergraduate final project he immediately accepted me into his group. He provided guidance, assistance, and most of all patience. He works throughout the week and, all too often, over the weekend to keep us all motivated, focused, and most of all: funded! Thank you for easing the process and providing a buffer against the bureaucracy.

Thanks also go to my committee members, Dr. Huaping Liu, Dr. Patrick Chiang, Dr. Raviv Raich, and Dr. Adam Schultz, for giving their valuable time and energy. I thank the staff members of the EECS department for their time, and the administrators of the Laurels Scholarship and the Rickert Engineering Fellowship for their generous donations.

Thanks to Ruiqing Ye, Charles Hu, Jin-jin He, Brad Nelson, Johannes Huschle, Seung-jin and Sang-jun, and Samia El-Amrani for working with me through the difficult projects, and all the rest of the group for giving valuable advice when I needed it.

I would also like to thank Boeing Company and Intel for their assistance and guidance in all ways. Without them, this would be a decidedly different thesis. Finally I would like to thank my family, blood and otherwise. Without my wife, I would never have considered graduate school, much less had the drive to continue

forward through thick and thin. The support and motivation I received from all my family encouraged me to strive forward intellectually and supported me throughout the adventure. But who will it be that will calculate my XP?

TABLE OF CONTENTS

	<u>Page</u>
1 Introduction	1
1.1 Motivation for Application	3
1.2 Challenges of Wireless Interconnects	4
1.3 Ultra-wideband Impulse Radio	5
1.4 Thesis Structure	5
2 UWB Channel Modeling	6
2.1 Frequency-Domain Channel Sounding	7
2.2 The Generic UWB Channel Model	8
2.2.1 Excluding antenna effects	9
2.2.2 $\frac{1}{d^n}$ path-loss model	10
2.2.3 Frequency-dependence of path-loss	13
2.2.4 Modified S-V model	13
2.2.5 Block fading	18
2.2.6 Root mean square (rms) delay spread	18
3 In-Chassis Channel Model	20
3.1 Propagation Path Loss	21
3.1.1 Measurement setup	22
3.1.2 Parameter extraction	24
3.1.3 Model parameters and comparison	29
3.2 Channel Impulse Response	30
3.2.1 Measurement setup	32
3.2.2 Parameter extraction	37
3.2.3 Model parameters and comparison	43
4 Pulse Response	45
4.1 UWB Pulser	47
4.1.1 Schematic design	47
4.1.2 Printed circuit board design	55
4.2 UWB Receiver	60
4.2.1 Schematic design	61
4.2.2 Printed circuit board design	65

TABLE OF CONTENTS (Continued)

	<u>Page</u>
4.3 Results	67
4.4 Future Development	69
5 Conclusion	70
Bibliography	71

LIST OF FIGURES

<u>Figure</u>	<u>Page</u>
1.1 FCC UWB spectral mask versus Part 15 Limit.	2
1.2 JTAG pin usage.	4
2.1 Frequency-domain channel sounding using VNA.	8
2.2 Comparison between far-field propagation and actual EM propagation.	12
2.3 Saleh-Valenzuela Cluster and Ray Decay.	16
3.1 Channel propagation path loss measurement diagram.	23
3.2 Channel Propagation path loss measurement flow chart.	24
3.3 Visual determination the path loss breakpoint.	25
3.4 Propagation path loss measurement data versus extracted model.	27
3.5 Frequency-dependent path loss measurement versus model.	28
3.6 Ideal original transfer function versus sampled transfer function.	31
3.7 Hermitian signal processing CIR derivation flow chart (from [1]).	32
3.8 Antennas in matched boresight configuration.	33
3.9 Recommended CIR measurement setup (from [2]).	34
3.10 CIR measurement setup.	35
3.11 Channel impulse response measurement flow chart.	36
3.12 Channel ray decay measurement versus model.	39
3.13 Channel cluster decay measurement versus model.	40
3.14 Measurement-derived cdf versus modeled cdf for two random bins.	42
4.1 Radiation pattern of professed omnidirectional UWB antenna (from [3]).	46
4.2 Ideal UWB pulse.	48
4.3 Frequency spectrum of ideal UWB pulse versus FCC spectral mask.	48

LIST OF FIGURES (Continued)

<u>Figure</u>		<u>Page</u>
4.4	Basic nanosecond pulse generator.	50
4.5	Equipment-generated subnanosecond pulse and BPF'd counterpart.	51
4.6	Frequency spectrum of BPF'd equipment-generated UWB impulse.	52
4.7	UWB pulser baseband generator schematic.	53
4.8	UWB pulser passband generator schematic.	54
4.9	Recommended 4-layer board stackup for maximum EM-shielding.	56
4.10	Stripline controlled-impedance line.	57
4.11	Board-edge and trace-lining stitching.	57
4.12	UWB pulser baseband generator PCB layout.	58
4.13	UWB pulser baseband generator PCB layout.	59
4.14	UWB pulser output pulse.	59
4.15	Typical non-coherent receiver.	60
4.16	UWB receiver stage 1 schematic.	63
4.17	UWB receiver stage 2 schematic.	64
4.18	UWB receiver stage 1 PCB layout.	65
4.19	UWB receiver stage 2 PCB layout.	66
4.20	Receiver output with near-ideal input.	66
4.21	Comparison of complete system outputs with computer turned off and on.	68

LIST OF TABLES

<u>Table</u>		<u>Page</u>
1.1	FCC Indoor UWB EIRP Mask.	3
2.1	List and Descriptions of Path Loss Parameters.	14
2.2	List and Descriptions of Impulse Response Parameters.	19
3.1	Channel Model Path Loss Parameters.	29
3.2	Channel Model Impulse Response Parameters.	43

DEDICATION

To my wife Ginny, for keeping me sane and happy forevermore. To my nuclear family, for raising me such that academic excellence was motivation in and of itself. And to my extended family, for the modifiers...

1 – Introduction

Traditionally in wireless communications, information signals are transmitted via one or a series of narrowband channels. From the basic Amplitude Modulation (AM), wherein the information signal is multiplied by a carrier sine wave, to Gaussian Minimum Shift Keying (GMSK), a form of frequency shift keying where the difference in frequency between a logical 'one' and 'zero' is exactly half the data rate, the vast majority of signals consist of a large average power concentrated over a small bandwidth. However, with the increase in global usage of wireless technologies, the wireless spectrum is becoming massively overpopulated. This profusion of signals has led to innovation in the form of Ultra-Wideband (UWB) transmission.

The concept of UWB is to replace the standard narrowband signal with an extremely wideband signal radiating a smaller average power. More specifically, to be classified as UWB, a signal must have either a bandwidth of at least 500 MHz or a fractional bandwidth $\sigma = B_w/f_C$ of at least 0.2, where f_C and B_w are the carrier frequency and signal bandwidth respectively. While it may seem counterintuitive to make up for a shortage of bandwidth by using a technology where bandwidth is increased, it is important to note that the allowed radiated power of a UWB system is not to exceed the FCC Part 15 Limit, the maximum transmit power for electrical equipment that is not designed to radiate. Table 1.1 and Figure 1.1

contain exact limits for UWB devices. Note that these numbers are in terms of the Effective Isotropic Radiated Power (EIRP), the amount of power required for an ideal isotropic antenna to emit peak power equivalent to the given application's antenna in its direction of maximum gain. A brief overview of UWB communi-

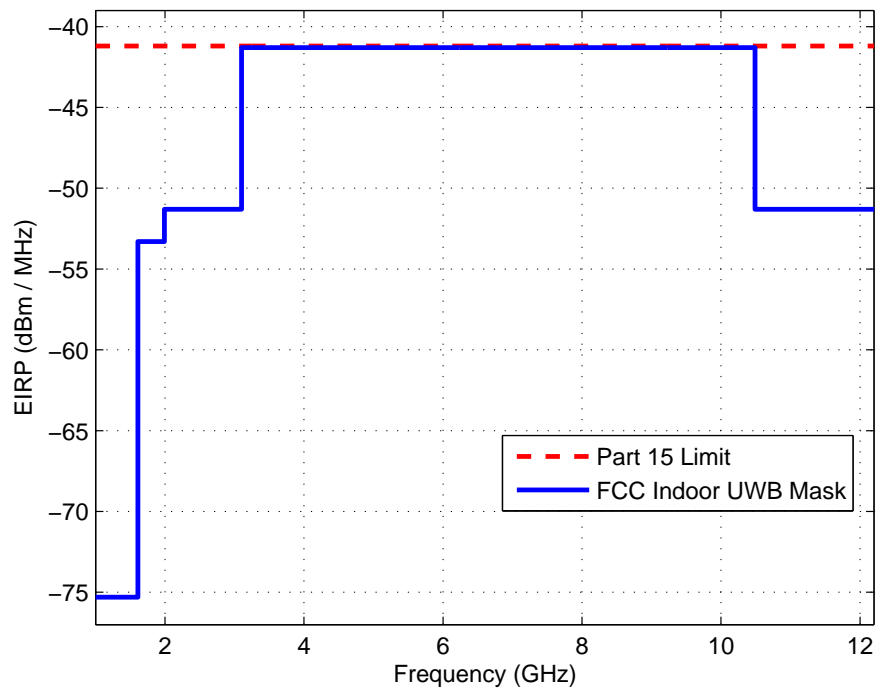


Figure 1.1: FCC UWB spectral mask versus Part 15 Limit.

cation techniques and systems can be found in [1, 4–7]. This thesis will focus on one major application for UWB technologies, the replacement of traditional wired interconnects in PC systems with a broadcast wireless system.

Frequency (MHz)	EIRP (dBm/MHz)
960 → 1610	-75.3
1610 → 1990	-53.3
1990 → 3100	-51.3
3100 → 10600	-41.3
10600+	-51.3

Table 1.1: FCC Indoor UWB EIRP Mask.

1.1 Motivation for Application

The modern computer is a device which, over the past few decades, has experienced remarkably sustained developmental progress, especially in terms of data processing. Unfortunately, a side-effect of such progress is a susceptibility to design artifacts in areas not considered of primary importance. A Joint Test Action Group (JTAG) daisy-chain [8], requiring multiple pins per component and routing between every chip in its chain, is one such artifact among many.

Restructuring chip-to-chip interconnects by replacing traditional wired systems with broadcast wireless would enable computer manufacturers to reap multiple benefits in terms of test and debug cost and reliability. A typical JTAG scan-chain is used to manipulate external and internal interfaces to test for faults, including part defects, connectivity failures, and on-chip logic issues. As shown in Figure 1.2 it uses between four and five pins on each chip to implement this useful functionality. Modern computing chips are, however, becoming smaller, and output ports more valuable [9]. There is, therefore, a strong need to free up interface ports for other I/O usage. By replacing the JTAG scan chain with an embedded wireless system which is, by definition, orthogonal to the existing test structure, numer-

ous benefits can be achieved. Several pins per chip would be freed for additional I/O, routing space required to link each JTAG component together would be decreased, and faulty connections would no longer exist, reducing the occurrence of incomplete and erroneous test results [10].

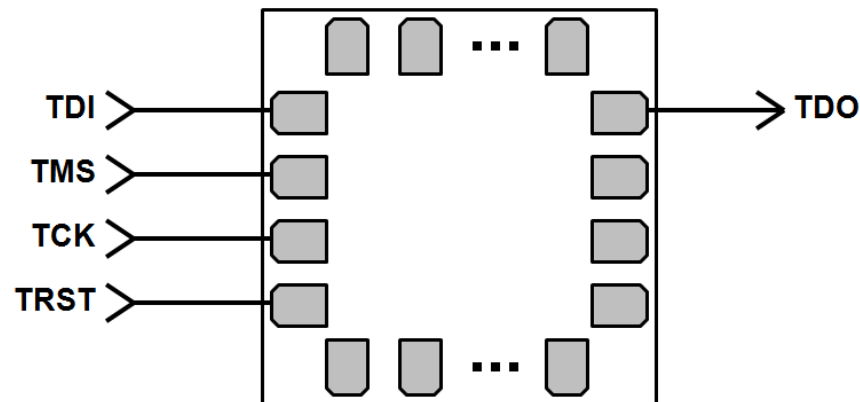


Figure 1.2: JTAG pin usage.

1.2 Challenges of Wireless Interconnects

The physical structure of the inside of a computer, where the system as described in Section 1.1 would exist, creates numerous challenges. Computer chassis are normally of small size and metal construction, primarily aluminum, which is highly reflective of electro-magnetic (EM) radiation, and thus extremely dense multipaths exist in this environment. Additionally due to the close proximity of these chips, a mixture of near-field and far-field propagation scenarios would result. The wireless communications scheme chosen for this environment has to be extremely resilient to multipath, operate well at short distances, be amenable to multi-user scenarios,

and as with all communication devices consume as little power as is feasible.

1.3 Ultra-wideband Impulse Radio

Ultra-Wideband Impulse Radio (UWB-IR) is a technology where a series of very short baseband impulses is amplitude modulated by a carrier frequency to form the UWB signal. This method is viable in a wide range of applications, from high-data-rate communication [11] to precise localization [12]. Characteristics of UWB-IR include resiliency to multipath, fine time resolution, and short range [4]. Due to its high bandwidth, UWB-IR can also work with multiple users [6], and can be implemented with low-power considerations [4]. For these reasons UWB-IR will be used as the system model for our implementation.

1.4 Thesis Structure

A brief review of literature pertinent to UWB channel modeling techniques and existing UWB channel models will be presented in Chapter 2, followed by an analysis and recommendations on UWB channel modeling methods. A comprehensive line-of-sight (LOS) channel model will be derived for the use within computer systems in Chapter 3. This model will then be analyzed to discern possible limitations for system implementation. Subsequently, the UWB pulse response of a system implemented in the channel of interest will be derived through use of a UWB pulser and receiver in Chapter 4, with conclusions being presented in Chapter 5.

2 – UWB Channel Modeling

Channel models for mobile cellular communications have been extensively studied, but for general UWB environments there has been less, but still significant, research. For example, personal area networks [13], automotive [14], high-rise apartments [15], indoor office [2], indoor residential [16], and industrial [17] environments have all been accurately characterized based on diverse methods. More recently, numerous efforts have been focused on modeling UWB channels [2, 13–22] and 60 GHz networks [23–26]. The most comprehensive contribution is the development of the IEEE 802.15.4a standardized UWB channel model [18], which compiled models characterizing myriad UWB environments. Despite this large quantity of descriptive channel models, there is no existing effort valid for the channel within a computer. The UWB channel final report can be used as a rough guideline for channel models, but the derivation of the actual parameters is only briefly discussed, leaving the methods of extraction primarily to the group creating the model. Also, these channel models are intended to be as general as possible, thus they ignore the effects of the transmission system used within the channel. Also available recently are a number of rough methods for generating a UWB-IR pulse [27–30], some with embedded on-chip antennas [31], as well as the design of UWB receivers for functions from low-data-rate communications [32] to ranging [33], using ultra-fast energy detectors [34], and even soft-limiting algo-

rithms [35]. These implementations vary widely, but unfortunately almost solely exist for the IC level, ensuring an astounding prototyping cost, and are for the most part not available for purchase. They are therefore of limited use in understanding a wireless channel.

The first consideration when generating a channel model for a specific environment is what method will be used. Because of the wide bandwidth of UWB systems, a channel model using time-domain channel sounding is impractical. In order to observe the entire frequency spectrum of interest, an ultra-short windowed impulse with approximately flat average power over multiple GHz must be generated. The generation of this impulse is prohibitively difficult. The frequency-domain channel sounding method has been shown to meet the requirements of a UWB channel [2, 13–19] and will be used in this thesis.

2.1 Frequency-Domain Channel Sounding

The frequency-domain channel sounding method is to construct a series of short-duration sinusoidal signals $s(t) = \cos(2\pi f(t))$ where $f(t)$ is a stair-step function which varies between the bounds f_{start} and f_{stop} of the frequency spectrum of interest; $s(t)$ is then transmitted through the channel of interest and the received signal $r(t)$ is analyzed to determine the change in amplitude due to channel distortion for each stair-step frequency value of $f(t)$. The difference in frequency steps $\Delta f = \frac{f_H - f_L}{N}$ can be adjusted depending on the equipment used for the measurements, where f_H, f_L and N are the upper and lower bounds of the frequency

spectrum of interest and the number of chirps, respectively. The output is therefore a frequency-domain plot of the distortion of a frequency-domain window function over the spectrum of interest. The channel impulse response (CIR) can then be calculated by taking the inverse Fourier transform (IFT) of the resultant frequency spectrum. This method is easily implemented through use of a Vector Network Analyzer (VNA) as shown in Fig 2.1.

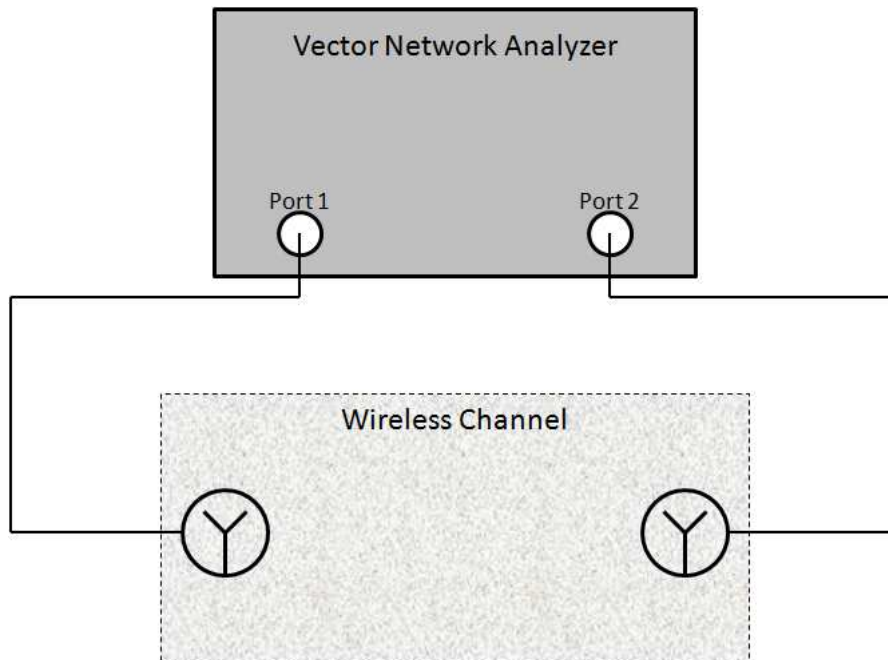


Figure 2.1: Frequency-domain channel sounding using VNA.

2.2 The Generic UWB Channel Model

It is also important to choose a structure for the channel model that coincides with the aspects of the channel of interest. In [18] it is given that the generic model for

multipath UWB channels should be as follows:

- Model addresses only the channel, excluding antenna effects
- Path-loss is modeled using $\frac{1}{d^n}$ model
- Frequency-dependence of path-loss is included
- Impulse response is characterized by a modified Saleh-Valenzuela (S-V) [36] model
 - Individual rays arrive in clusters of approximately equal time-delay
 - Ray arrival is characterized by a mixed Poisson distribution
 - Interdependence of cluster inter-arrival times
 - Small-scale fading characterized as a Nakagami distribution with m -factors as a random variable
- Channel remains constant for the duration of the measurement period (Block Fading)

2.2.1 Excluding antenna effects

Because the standard VNA measurement of the channel as shown in Figure 2.1 does not eliminate the effects of the antenna on the model intended only for the channel, a method must be implemented to minimize the impact of antenna distortion on the measured received power. One accepted method for this is to deconvolve the

antenna gain from the received power spectrum. This is an extensive process which employs a modified version of the CLEAN algorithm [37] to selectively remove one arrival ray at a time from the received CIR. While this method was applied for a UWB channel in [38], the extraordinarily dense multipath of the channel of interest makes for exceptionally short ray inter-arrival times. The time-domain resolution afforded by the available VNA is simply inadequate for the CLEAN algorithm. To approximate the elimination of antenna characteristics, the antennas were placed in a free-space approximation and their contribution to the received spectrum was calibrated out using the VNA calibration process. In this way both the antenna's directional efficiency and its frequency-dependence can be accounted for without increasing processing time.

2.2.2 $\frac{1}{d^n}$ path-loss model

The distance-dependent path loss (DDPL) of a channel is derived from the modified Friis' equation (2.1) as follows, where P_t , P_r , G_t , G_r are the transmitted and received power, and transmitting and receiving antenna gains, respectively, λ is the wavelength of the signal, and d and n are the distance between the transmitting and receiving antennas and the experimentally determined path loss exponent, respectively:

$$P_r = P_t G_t G_r \left(\frac{\lambda}{4\pi d} \right)^2 \left(\frac{1}{d} \right)^n \quad (2.1)$$

Substituting normalized gain in the transmitter and receiver, setting the transmitted power to equal one, and substituting $\lambda = c/f$ this can be simplified to (2.2)

for the path loss $L(d)$.

$$L(d) = \left(\frac{c}{4\pi df} \right)^2 \left(\frac{1}{d} \right)^n \quad (2.2)$$

Since the channel path loss cannot be measured at a distance of zero, a reference distance d_0 appropriate to the environment must be determined. The calculated path loss will then be in reference to the loss L_0 at d_0 . Taking the logarithm, the path loss equation can be simplified as (2.3).

$$L(d)(dB) = L_0 - 10n \log_{10}(d/d_0) \quad (2.3)$$

Path loss values generally fall near, but not on, the log-line described by this equation [15,39]. The difference between the calculated value for $L(d)$ and the measured value is called a *shadowing component*, and is assumed to be a zero-mean Gaussian random variable with standard deviation of σ_S .

As stated in Section 1.2, the channel of interest will experience both near-field and far-field propagation. In [20], Schantz demonstrates that the path gain of a near-field/far-field channel is characterized by two distinct path loss exponents. He states that the path loss of an electromagnetic signal has a transition distance between one-tenth and one-half the wavelength of the signal, where the path loss exponent substantially decreases. A comparison between assumed far-field propagation and actual EM propagation can be seen in Figure 2.2. To account for this factor, the included path loss model is broken into two segments, where the transition distance is determined experimentally. This gives the final DDPL model: (2.4).

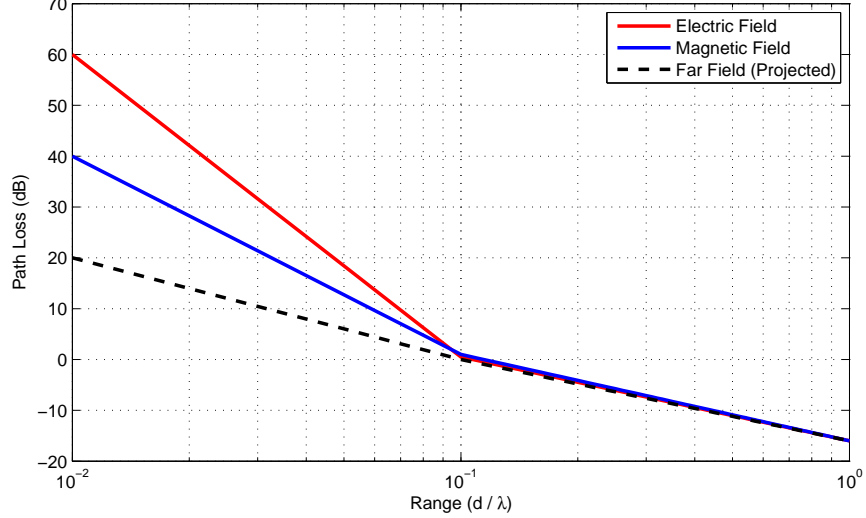


Figure 2.2: Comparison between far-field propagation and actual EM propagation.

$$L_{dB}(d) = \begin{cases} L_{01} + 10n_1 \cdot \log_{10}(d/d_{01}) + S_1, & d_{01} < d \leq d_{02} \\ L_{02} + 10n_2 \cdot \log_{10}(d/d_{02}) + S_2, & d > d_{02} \end{cases} \quad (2.4)$$

In this model d_{02} is the field transition distance: when $d_{01} < d \leq d_{02}$ propagation is a near-field scenario; when $d > d_{02}$ propagation is far-field. L_{01} is the loss at the reference distance d_{01} , L_{02} represents the path loss at the transition distance d_{02} , n_1 and n_2 are the near-field and far-field path gain exponents, respectively, and S_1 and S_2 are the near-field and far-field shadowing components with corresponding standard deviations σ_{S1} and σ_{S2} in dB.

2.2.3 Frequency-dependence of path-loss

For narrowband systems, the frequency dependence of path loss is normally ignored. Because of the high bandwidth of UWB systems, however, this factor must be taken into account. Evidence is presented in [15] that the frequency dependency of the path loss can be adequately modeled as (2.5), with frequency decaying factor κ . This method is also adopted in [18], and will be used in this model.

$$\sqrt{L(f)} \propto f^{-\kappa} \quad (2.5)$$

The total path loss is therefore the combination of the distance-dependent (2.4) and frequency-dependent (2.5) path loss formulas as presented in (2.6) [19]. The full list of path-loss parameters is shown in Table 2.1.

$$L(f, d) = L(f) \cdot L(d) \quad (2.6)$$

2.2.4 Modified S-V model

As presented in [36], the Saleh-Valenzuela complex baseband model for an indoor multipath impulse response can be expressed as (2.7). The variable l is the cluster index, k denotes the k^{th} ray of the l^{th} cluster, $\beta_{k,l}$ is the path gain of the k^{th}

Table 2.1: List and Descriptions of Path Loss Parameters.

Parameter	Description
L_{01}	Path loss at distance d_{01}
d_{01}	Reference distance
L_{02}	Path loss at distance d_{02}
d_{02}	Near-field to far-field transition distance
n_1	Near-field path loss exponent
n_2	Far-field path loss exponent
σ_{S_1}	Near-field shadowing standard deviation
σ_{S_2}	Far-field shadowing standard deviation
κ_1	Frequency dependence of the path loss (near-field)
κ_2	Frequency dependence of the path loss (far-field)

path of the l^{th} cluster, $\tau_{k,l}$ is the delay of the k^{th} path of the l^{th} cluster relative to the l^{th} cluster arrival time T_l , and $\theta_{k,l}$ is the component phase, which is uniformly distributed over $[0, 2\pi]$.

$$h(t) = \sum_{k,l} \beta_{k,l} \cdot e^{j\theta_{k,l}} \cdot \delta(t - T_l - \tau_{k,l}) \quad (2.7)$$

In order to better understand this equation, it must be broken down. First we observe that it is a double summation over k and l as defined above. Upon observation of a physical multipath environment, it becomes clear that reflections do not have a uniformly distributed inter-arrival time. Since antennas are not point devices, multiple rays reflected through *similar paths* would stimulate an electrical reaction in the antenna element at close to, but not exactly, the same time. On a CIR, this would appear as a group of time-delayed impulses, known as a *cluster*. Due to the existence of electromagnetically-reflecting materials in the

channel, there exists more than one significant path from transmitter to receiver. This results in a series of clusters arriving with different time delays. It is logical to account for each of these clusters separately in the CIR equation. In (2.7), the clusters are numbered $l = 0 \rightarrow \infty$, and each individual ray per cluster (modeled as a dirac delta function) is indexed $k = 0 \rightarrow \infty$. The CIR would therefore be the summation over k and l of each arriving ray, delayed by the time to its cluster's arrival T_l and the difference in time between the cluster's arrival and the individual ray's arrival $\tau_{k,l}$. Since each ray experiences unique reflections, it is assigned a phase shift value $\theta_{k,l}$ accordingly. Finally, since the path of each ray differs from that of every other, its amplitude value is also uniquely assigned as $\beta_{k,l}$.

2.2.4.1 Power Delay Profile

From equation (2.7), random variables can be extracted for use in modeling the behavior of the channel of interest. Considering first the individual ray magnitudes, it is clear that since a time delay translates directly to a longer path of travel, accounting also for imperfect reflection coefficients, the later-arriving rays from each cluster would have exponentially decreasing amplitudes. A cluster therefore would take the shape of a sharp peak followed by an exponential decay as in Figure 2.3 [36]. Intra-cluster exponential decay factor γ is used to estimate this behavior. Variance from this value is considered in Section 2.2.4.2. Since the arriving rays are so densely packed, it is prohibitively difficult to resolve individual ray arrivals. Instead, ray arrival rates are modeled using a tapped delay-line with regularly

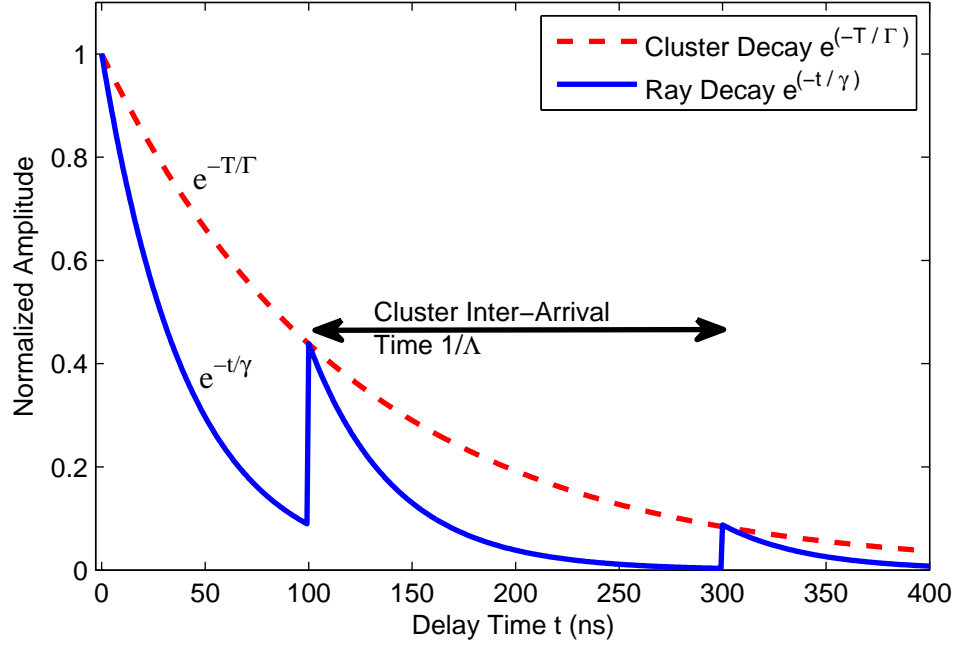


Figure 2.3: Saleh-Valenzuela Cluster and Ray Decay.

spaced taps [19].

Arriving clusters can be modeled similarly to arriving rays. Clusters which traverse longer paths would experience similar attenuation such that the peak values for each cluster would also show an exponential decay. Since each cluster is adding on to the residual energy of clusters preceding it, they can be readily distinguished from the CIR as in Figure 2.3. Inter-cluster exponential decay factor Γ estimates this behavior [36]. As with path loss there is some variance from this projection, so a Gaussian zero-mean cluster shadowing factor M_{cluster} is used, which is fully described by its variance σ_{cluster} . The mean energy of the l^{th} cluster is therefore

described [18] by (2.8).

$$10 \log (\Omega_l) = 10 \log [\exp (-T_l / \Gamma)] + M_{\text{cluster}} \quad (2.8)$$

In [18, 36] it is shown experimentally that the distributions of the time delay between clusters are given by Poisson processes as (2.9). Cluster inter-arrival rate Λ fully describes this process. Finally, the number of clusters L has been observed [18] to be Poisson distributed with probability density function (pdf) (2.10) and is fully characterized by its mean \bar{L} .

$$p(T_l | T_{l-1}) = \Lambda_l \exp [-\Lambda_l (T_l - T_{l-1})], \quad l > 0 \quad (2.9)$$

$$pdf_L(L) = \frac{(\bar{L})^L \exp (-\bar{L})}{L!} \quad (2.10)$$

2.2.4.2 Small-scale fading

At this point the S-V model has been parameterized for all factors except small-scale component weights $\beta_{k,l}$. In [36] it is suggested that several distributions may be able to describe this factor. Rayleigh [40], log-normal [41], and a Gaussian wide-sense stationary uncorrelated scattering (GWSSUS) [42] models are all suggested. For narrowband channels, the first multipath component behaves as Rician or Nakagami, with trailing components described by the Rayleigh distribution. In UWB channels, however, their behavior coincides much better with the Nakagami

distribution [2]. In this thesis the small-scale fading is modeled as Nakagami (2.11) with $m > 1/2$ as in [18], where $\Gamma(m)$ and Ω are the gamma function and the mean-square amplitude, respectively. The m -factor was found to be log-normally distributed and is fully described by its mean μ_m and variance σ_m .

$$pdf(x) = \frac{2}{\Gamma(m)} \left(\frac{m}{\Omega}\right)^m x^{2m-1} \exp\left(-\frac{m}{\Omega}x^2\right) \quad (2.11)$$

2.2.5 Block fading

In this thesis, measurements were taken in an EM-shielded laboratory with no localized radio frequency (RF) signals in evidence other than the signal of interest. For the duration of each measurement period there was no movement within the channel or surrounding areas. Block fading is thus in evidence.

2.2.6 Root mean square (rms) delay spread

Another concept which is useful in understanding the impulse response of a channel and its practical applications is the rms delay spread τ_{rms} . The maximum delay spread is a factor which describes the time difference between the arrival of the first and last significant rays due to a single transmitted impulse. The rms delay spread, being the energy-weighted standard deviation of the ray delays, can be found as (2.13) [21] from the second moment of the power-delay profile $P(\tau)$ with peaks a_k^2 and is generally used to determine the shortest time delay between transmitted symbols such that inter-symbol interference (ISI) is minimized. This parameter

has been found to vary with distance [21], but since the maximum transmission distance in the channel of interest is short, a mean value for $E\{\tau_{rms}\}$ is sufficient to characterize this factor. The full list of impulse response parameters is shown in Table 2.2. Note that all of these parameters will be constructed both for near-field and far-field scenarios.

Table 2.2: List and Descriptions of Impulse Response Parameters.

Parameter	Description
Λ	Cluster inter-arrival rate
\bar{L}	Mean number of ray clusters
Γ	Inter-cluster decay time
γ	Intra-cluster decay time
σ_{cluster}	Cluster shadowing deviation
μ_m	Small-scale fading m -factor mean
σ_m	Small-scale fading m -factor deviation
$E\{\tau_{rms}\}$	Mean rms delay spread

$$\tau_{rms} = \sqrt{\overline{\tau^2} - (\bar{\tau})^2} \quad (2.12)$$

$$\overline{\tau^2} = \frac{\sum_k a_k^2 \tau_k^2}{\sum_k a_k^2} \quad (2.13)$$

$$\bar{\tau} = \frac{\sum_k a_k^2 \tau_k}{\sum_k a_k^2} \quad (2.14)$$

3 – In-Chassis Channel Model

In Chapter 2 the format of the included model was presented. This established, the next step when constructing a channel model is the actual measurement process. Any accurate channel model must be based on a statistically significant number of measurements to provide assurance of the correctness of derived parameters. Additionally, these measurements must be taken in a static environment where such factors as human body proximity [18] and external interference are minimized or eliminated. The environment measured is the inside of a typical computer chassis measuring $45 \times 20 \times 40$ cm². To most accurately characterize the channel during normal operation, all miscellaneous components (hard disk drives, power cables, etc.) were left inside the chassis for the duration of the measurements. This chassis was placed in an EM-shielded lab. The environment surrounding the chassis resembled a typical usage scenario for a home computer, with the exception of the operating user. The nearest human proximity was stationary at eight meters, 20 times the distance characterized by this model. Modeled parameters are extracted using established methodologies [18,43] by implementing best-fit algorithms on the captured data. Due to the limitations of the antenna used during measurements, the model presented herein is valid for the 3 - 6 GHz frequency range. Because of the size of the typical computer chassis, distances were limited to 1 - 40 cm. The antenna used in the channel model was the Skycross SMT-3TO10M-A [44].

3.1 Propagation Path Loss

For the propagation path loss portion of the model, a VNA was used as described in Section 2.1 to capture 1601 data points between 3 - 6 GHz. This provides a frequency-domain resolution of 1.875 MHz. Captured data was analyzed in the frequency domain. Section 2.2.3 asserts that a UWB channel's path loss varies with both frequency and distance. A method must be established to isolate these dependencies as in (2.6) so that parameters can be extracted properly. In [45], Ghassemzadeh shows that by averaging the sampled complex frequency-domain response over all frequencies, the impact of the frequency on the path loss can be discounted (3.1). For this equation N , f_i , d and $H(\cdot)$ are the number of frequency points sampled, the frequency values themselves, the distance at which the measurement took place, and the complex frequency-domain transfer function of the channel, respectively. The mean log-scale path loss at a distance d irrespective of frequency can therefore be found by taking the mean of a statistically significant number M of these frequency-averaged data sequences (3.2).

$$L(d) = \frac{1}{N} \sum_{i=1}^N (|H(f_i, d)|^2) \quad (3.1)$$

$$L_{dB}(d) = 10 \log_{10} \left[\frac{1}{NM} \sum_{i=1}^N \sum_{j=1}^M (|H(f_{i,j}, d)|^2) \right] \quad (3.2)$$

Having determined a method for eliminating the frequency-dependence to isolate the distance-dependence, one must now be found to isolate the frequency-dependence. In [43], a 30×30 cm² square of measurement points is rms-averaged

to eliminate the distance-dependence. This indicates that this method can be replicated in the channel of interest, albeit on a much smaller scale. This is accomplished by implementing (3.3) where N and d_i are the number of distance points sampled and the distance values themselves. The mean log-scale path loss at a frequency f can be found by calculating the rms-mean of a number m of these data sequences (3.4).

$$L^2(f) = \frac{1}{N} \sum_{i=1}^N (|H(f, d_i)|^4) \quad (3.3)$$

$$L_{dB}(f) = 5 \log_{10} \left[\frac{1}{NM} \sum_{i=1}^N \sum_{j=1}^M (|H(f, d_{i,j})|^4) \right] \quad (3.4)$$

3.1.1 Measurement setup

The method chosen in this thesis for the determination of propagation path loss parameters is very typical. Using the frequency-domain channel sounding method in Section 2.1, a VNA is connected with valid cables to two antennas, one each to Port 1 and Port 2 of the device as in Figure 2.1. One antenna is fixed, while the other is placed at varying distances d_i from the first, within the channel of interest. For this channel, a distance range of 1 - 40 cm was estimated from the usage scenario. Increments of 1 cm were used so that an approximate break-point could be resolved through measurement data. After data was taken at each of the 40 distance increments, the primary fixed antenna was repositioned and the measurement sequence repeated. Figure 3.1 shows the in-chassis antenna positioning setup. A flow-chart of the propagation path loss measurement process is shown in

Figure 3.2.

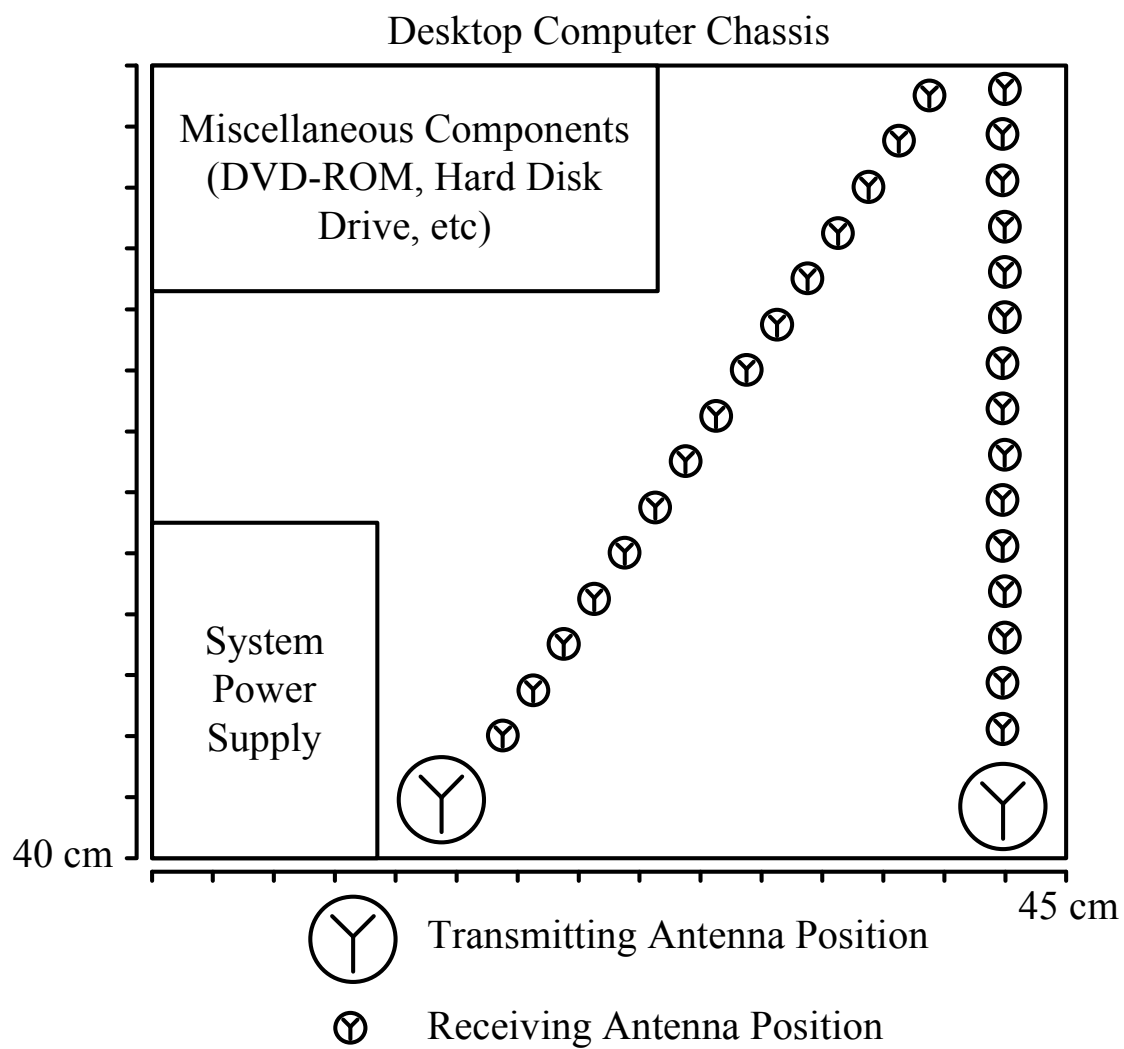


Figure 3.1: Channel propagation path loss measurement diagram.

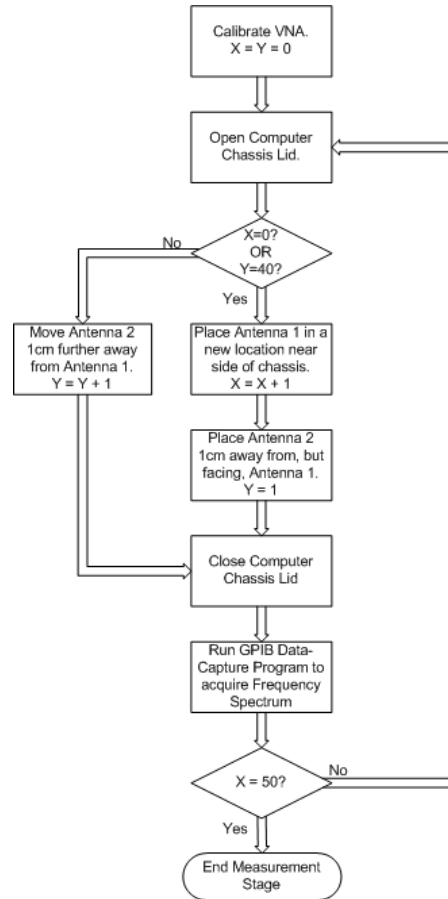


Figure 3.2: Channel Propagation path loss measurement flow chart.

3.1.2 Parameter extraction

In this section the process by which each path loss parameter was extracted is explained. These primarily follow the process suggested in [18] with the exception of d_{02} and κ ; d_{01} is defined as the shortest distance included in the model at 1 cm. Results are given and analyzed in Section 3.1.3.

3.1.2.1 d_{02}, L_{01}, L_{02}

The path loss L_{01} at reference distance d_{01} is quite simple to extract. Take the mean of the DDPL for all measurements at the reference distance using (3.2). The resultant value is assigned to L_{01} .

In order to find the breakpoint describing the division between near-field and far-field propagation, compute the mean DDPL value for each distance d_i as in (3.2). Plot the resultant values as data points in loglog-scale with respect to the measurement distances. By observation, find the distance point where the instantaneous slope $m_i = \frac{L_i - L_{i-1}}{d_i - d_{i-1}}$ of the path loss decreases dramatically as in Figure 3.3. The distance d_{i+1} corresponding to the last point before the slope decreases is the path loss breakpoint d_{02} . Because of the chosen distance resolution (1 cm) this approximate value will suffice. Once d_{02} is found, the value of the mean DDPL for this distance is the far-field reference loss L_{02} .

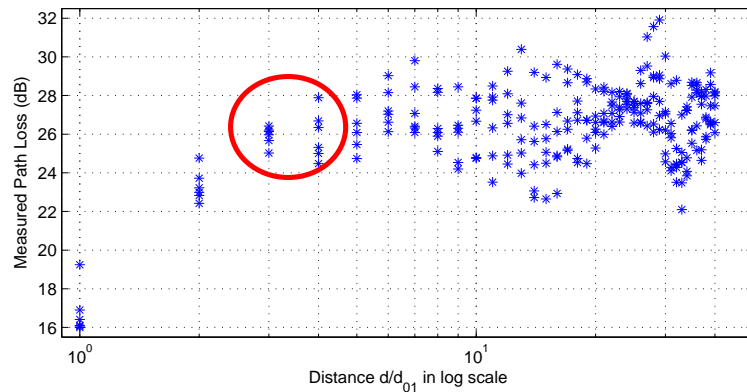


Figure 3.3: Visual determination the path loss breakpoint.

3.1.2.2 n_1, n_2

To find the near-field and far-field path loss exponents, first separate the measured data into two groups, one each for the log-scale DDPL at distances $d \leq d_{02}$ and $d > d_{02}$. For the near-field exponent, subtract L_{01} from all the loss values associated with near-field distances and use linear regression to find the slope of the best-fit model's linear approximation. For the far-field exponent, repeat this process on the loss values associated with far-field propagation, remembering to subtract L_{02} rather than the near-field reference loss. Note that the linear regression should be applied with both amplitude and distance in log-scale for each of the near-field and far-field cases. A plot of the extrapolated linear regression model for the channel of interest is shown in Fig 3.4.

3.1.2.3 σ_{S1}, σ_{S2}

To find the DDPL shadowing deviations, again use the measured loss values separated into near-field and far-field categories. Here define the error ΔL_j between an individual measured DDPL value at distance d_i enumerated by j and the estimated DDPL for that distance as in (3.5), where $V_{i,j}$ is a measured DDPL at distance d_i . Note that this value is irrespective of distance. Once ΔL_j is constructed, ensure that it is a Gaussian zero-mean variate, then find its standard deviation. The standard deviation for near-field distances is assigned to σ_{S1} , and the standard

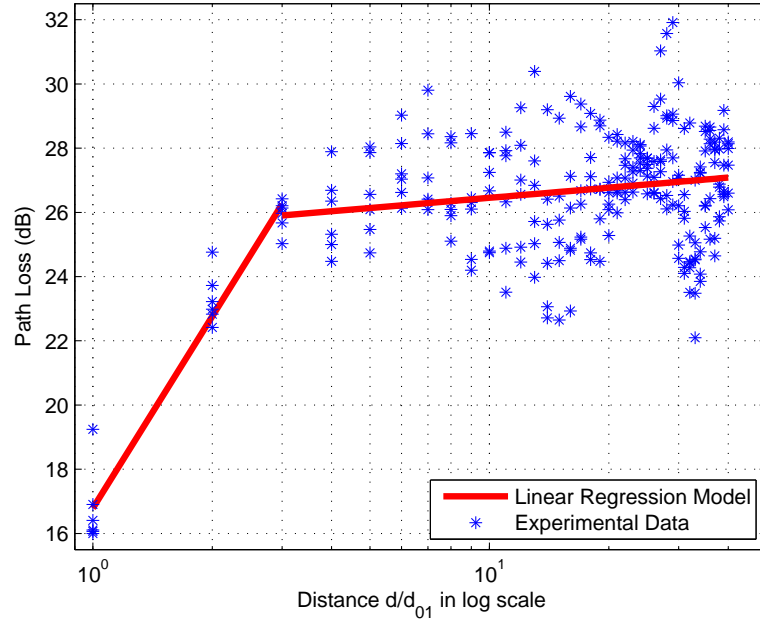


Figure 3.4: Propagation path loss measurement data versus extracted model.

deviation for far-field distances is assigned to σ_{S1} .

$$\Delta L_j = L_{dB}(d_i) - V_{i,j} \quad (3.5)$$

3.1.2.4 κ_1, κ_2

The extraction of the frequency-dependence of the path loss, κ , again begins with the separation of measurements into near-field and far-field. Since κ relies on the elimination of dependence on distance, this seems like an unnecessary step. However, since EM signals behave very differently in the near-field and far-field regions, it will be a good measure of the dependence-elimination method to compare the

two parameters, which should be approximately equal.

To determine the frequency-dependent loss function $L(f)$, take the rms-average of the measured values as in (3.4). Next, use linear regression where the arguments are the log-scale path loss versus a modified frequency axis $10 \log_{10}(f/f_0)$ where f_0 is the lowest frequency measured, 3 GHz in the case of this thesis. The quantity output as the slope of this log-linear approximation is a negative exponential $-|\kappa|$. Since κ is seen as a positive value, the absolute value of this becomes the frequency-dependence value κ . Repeat this procedure for both near-field and far-field situations and compare κ_1 and κ_2 to ensure they are similar. Figure 3.5 shows the best-fit model frequency-dependent path loss versus measured data taken from the channel of interest.

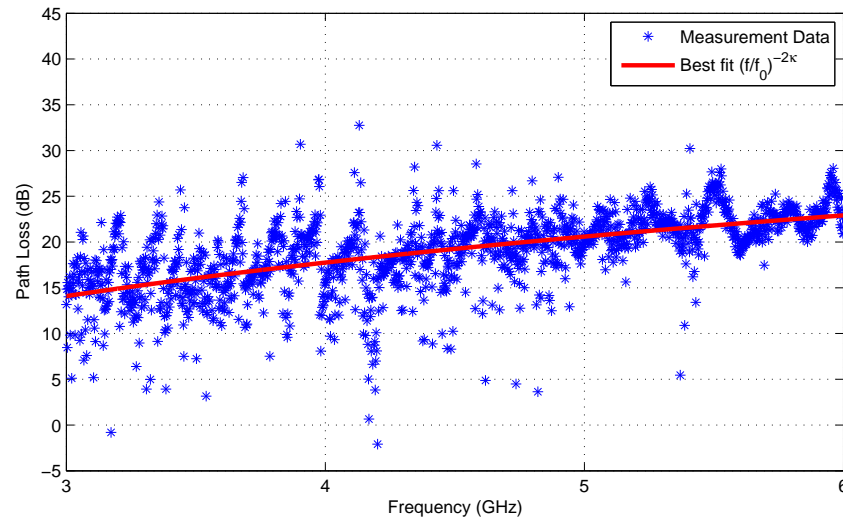


Figure 3.5: Frequency-dependent path loss measurement versus model.

3.1.3 Model parameters and comparison

Table 3.1 shows the parameters extracted by the specified instructions for the channel of interest. Note that κ_1 and κ_2 are similar in value. This verifies the method used to eliminate the distance-dependence of path loss (3.4). As expected,

Table 3.1: Channel Model Path Loss Parameters.

Parameter	Near-field	Far-field
Valid Range (cm)	1 to d_{02}	d_{02} to 40
i (for parameters below)	1	2
d_{0i} (cm)	1	3
L_{0i} (dB)	16.78	25.90
n_i	1.99	0.11
σ_{S_i} (dB)	0.94	1.67
κ_i	1.31	1.47

the path-loss breakpoint model accurately fits measurement data as shown in Figure 3.4. It is also observed that most of the channel parameters for the computer chassis environment differ considerably from those for indoor, residential, high-rise buildings, and industrial short-range communications environments [2, 13–19]. Most notably, the path-loss exponent for far-field propagation n_2 is significantly lower than in any existing literature. Such drastic differences are a result of the special environment. As explained in Chapter 3, this channel for ultra-short-range UWB communications is almost completely enclosed in electromagnetic-reflective materials. It stands to reason that, in such an environment, a portion of the energy dispersed by an omni-directional antenna will be reflected back toward a given receiver rather than continuing to propagate outward. The result of this is that the

amount of signal energy lost over distance is significantly less than the commonly accepted $1/r^2$ factor. The exponent for near-field path loss n_1 is much more ordinary, but when compared to the far-field loss exponent it is much greater. This is due to the increased path loss in near-field scenarios.

3.2 Channel Impulse Response

In order to extract the CIR parameters from the VNA measurement data acquired by the method in Section 2.1 and observe their correctness, it becomes necessary to derive an individual CIR from each measured frequency spectrum acquired through use of the frequency-domain channel sounding method. First, it is observed that the measured data is a one-sided, windowed version of the ideal transfer function of the channel where the frequency is offset by a constant. Fig 3.6 shows a comparison between the original transfer function $H(f)$ and the sampled transfer function $H_s(f)$. The inverse Fourier transform of this function (3.6), where r and k are the start and stop frequencies for the sampled spectrum respectively, would yield a distorted complex impulse response.

$$F^{-1} \{H_s(k)\} = \frac{1}{k-r+1} \sum_{k=N-r}^{N-k} H(k) e^{\frac{2\pi i}{k-r+1}(k-(N-r))n} \neq h(n) \quad (3.6)$$

In [1] it is suggested that an accurate real-valued CIR can be found using Hermitian signal processing. Following this method, the sampled spectrum is zero-padded from 0 Hz to the lowest sampled frequency, 3 GHz in this thesis. The

modified spectrum is then conjugate-reflected about the DC axis to provide a two-sided conjugate-symmetric frequency-domain approximation of the transfer function $H_H(f)$ to which the IFT can be applied (3.7), resulting in a real-valued CIR.

$$F^{-1} \{H_H(k)\} = \frac{1}{N} \sum_{k=0}^{N-1} H_H(k) e^{\frac{2\pi i}{N} kn} \approx h(n) \quad (3.7)$$

Figure 3.7 from [1] is a flow-chart representation of this process. This method

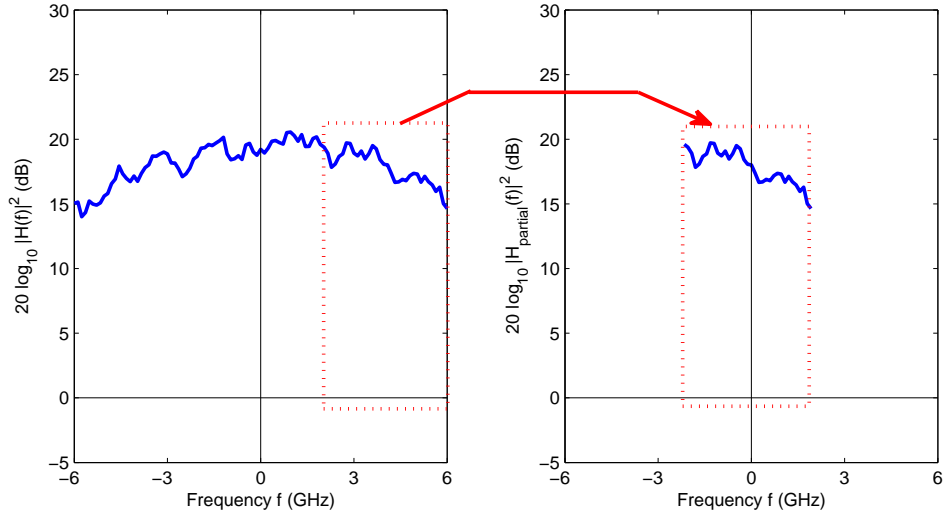


Figure 3.6: Ideal original transfer function versus sampled transfer function.

is used to find all CIR's used in the extraction of the following parameters. Note that since the model only needs to represent the effective paths, a cutoff factor was applied so that only paths less than $20dB$ below the highest received power were considered [18].

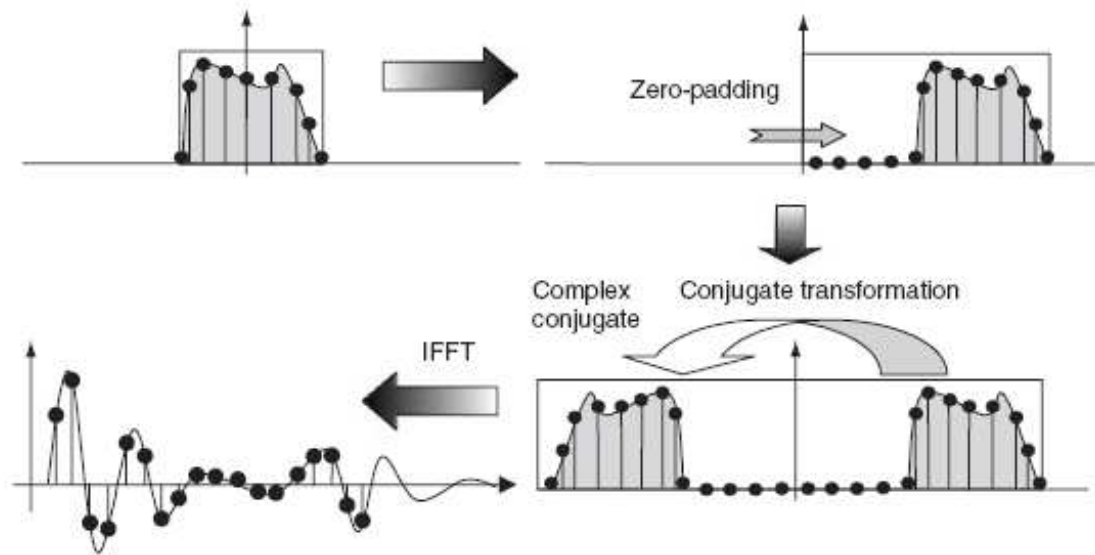


Figure 3.7: Hermitian signal processing CIR derivation flow chart (from [1]).

3.2.1 Measurement setup

The measurement setup for the CIR parameters of the channel model differs from the standard methodology presented in [46] because of the method used to eliminate the contribution of the antennas (Section 2.2.1). The VNA calibration was done including the antennas in matched boresight configuration as in Figure 3.8, so the relative directions of the antennas must remain static for the measurements to be valid. The recommended setup from [2] uses a series of square measurement grids spread throughout the channel of interest, shown in Figure 3.9. Because of the need to keep the boresights of the antennas aligned, this configuration is invalid for the process in this thesis. Instead, a new setup is defined as in Figure 3.10. In this process Antenna 1 is set in a fixed location with variable angle and Antenna 2 is placed along the radial lines of a circle with center point described

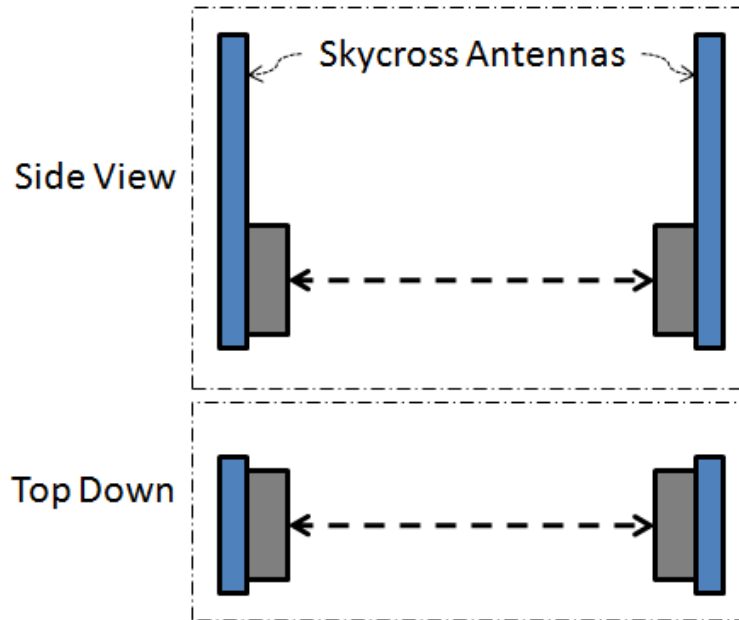


Figure 3.8: Antennas in matched boresight configuration.

by the position of Antenna 1. The antennas are rotated so that their boresights are always aligned. After the channel is sampled for a particular configuration, Antenna 2 is shifted along the radial line and Antenna 1 is rotated to face it, then the measurement process is repeated. Once sufficient data is collected for a certain radial line, Antenna 2 is shifted to another radial line. After several lines are sampled, Antenna 1 is repositioned and the process is repeated. This allows for groups of data used to analyze large-scale and small-scale fading factors. To analyze small-scale factors the collected CIRs within each radial line are examined and compared to the averaged CIR for their respective radial line. For large-scale factors the collected CIRs for each radial line are averaged, and these averages (one for each radial line) are examined. This is similar to the process in [2] except

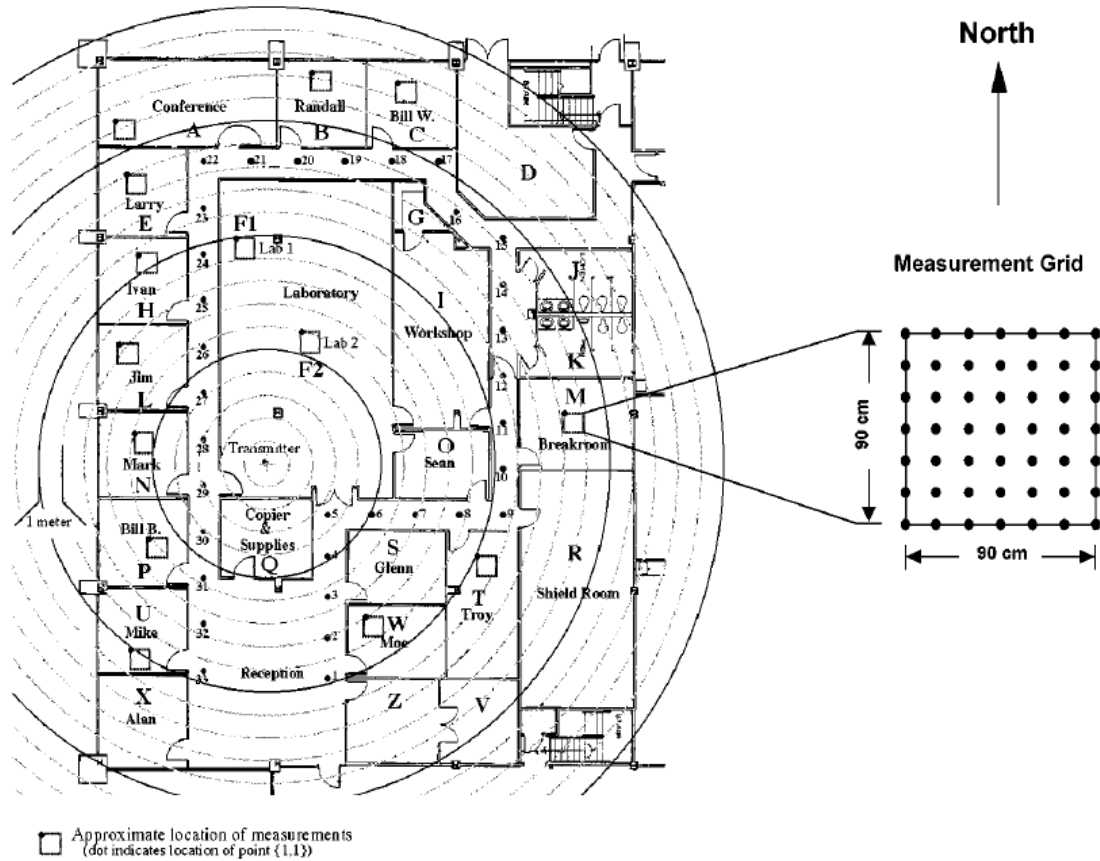


Figure 3.9: Recommended CIR measurement setup (from [2]).

for the use of radial lines rather than measurement grids. A flow-chart of the CIR measurement process is shown in Figure 3.11.

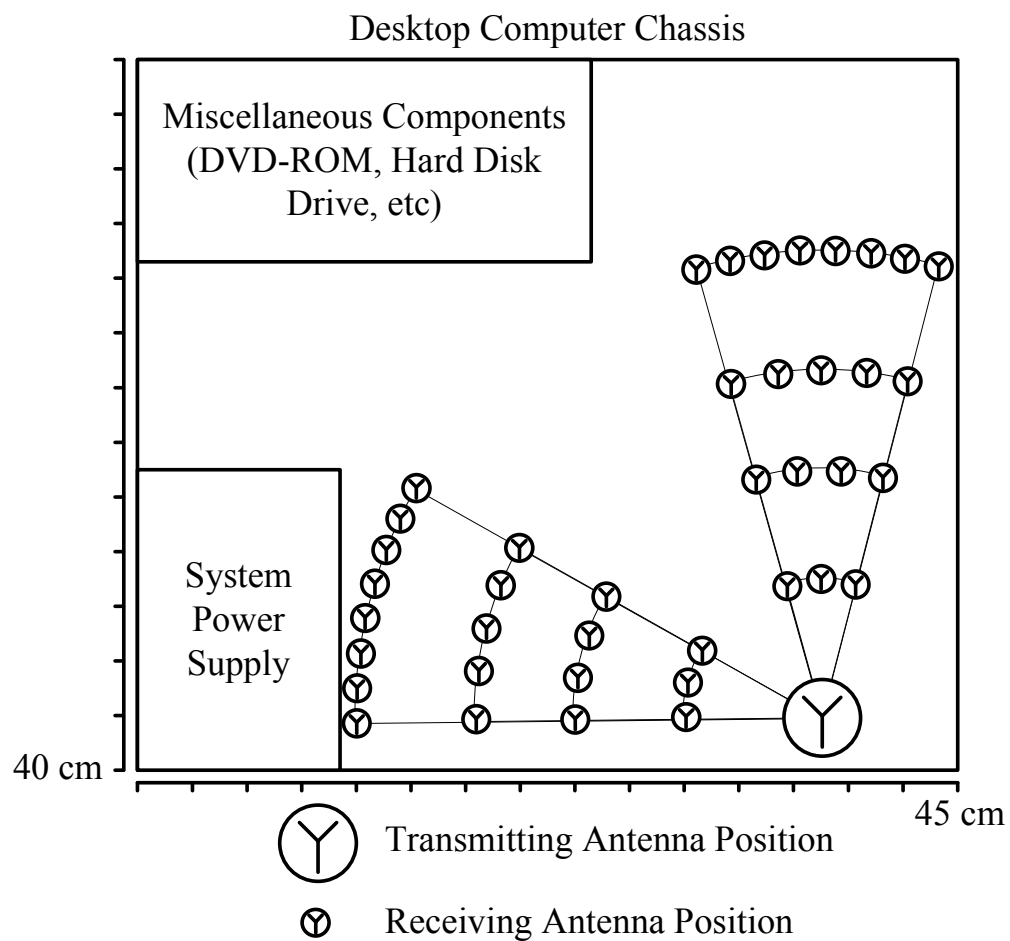


Figure 3.10: CIR measurement setup.

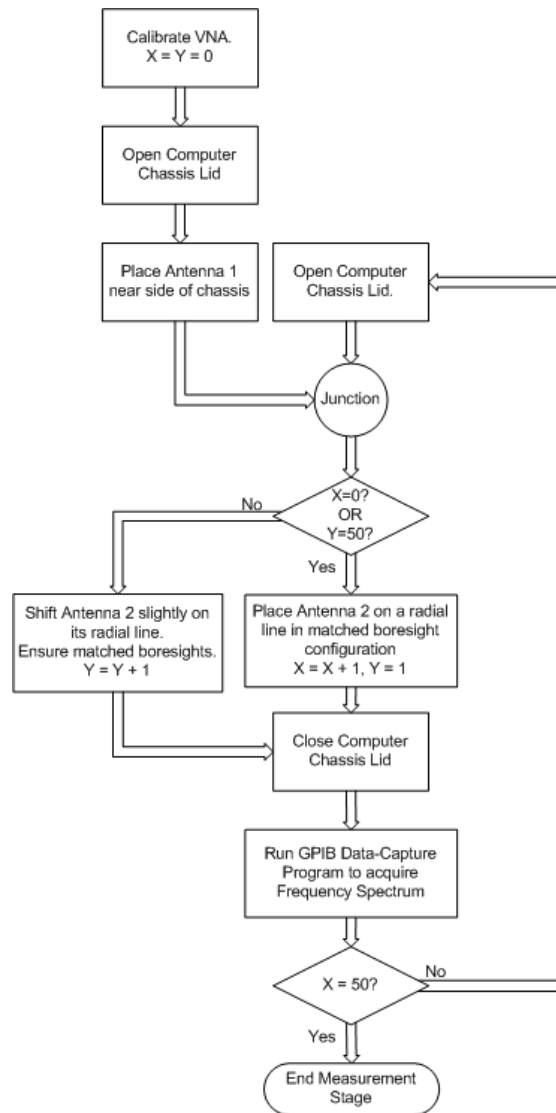


Figure 3.11: Channel impulse response measurement flow chart.

3.2.2 Parameter extraction

In this section the process by which each path loss parameter was extracted is explained. These primarily follow the process suggested in [18]. For each parameter, sampled data was separated into near-field and far-field groups, which were analyzed independently. Results are given and analyzed in Section 3.2.3.

3.2.2.1 \bar{L}

The mean number of clusters per CIR, \bar{L} , is a large-scale Poisson-distributed parameter. For this and all other large-scale factors, the first step should be to average the CIRs over their radial lines to eliminate the impact of small-scale fading. After this is done, identify cluster peaks within each CIR. It is very difficult [18] to develop an algorithm significantly robust to accomplish this, so visual inspection is implemented as recommended. Take note of the cluster peak index values for later use. Determine the total number of clusters in each CIR and take the mean value using maximum-likelihood estimator (MLE) of a Poisson-distributed random variable's mean (3.8). This is assigned to \bar{L} .

$$\bar{L}_{MLE} = \frac{1}{N} \sum_{k=1}^N (L_k) \quad (3.8)$$

3.2.2.2 Λ

The cluster inter-arrival rate, Λ , is a large-scale Poisson arrival rate. For each averaged CIR, find the times \underline{t} associated with each cluster's first (not peak) ray arrival. Construct an array, $\underline{\Delta t}$, of inter-arrival times by subtracting from each i th cluster arrival in each j th CIR, $t_{i,j}$, from the arrival time of the preceding cluster, neglecting the first cluster ($\Delta t_{i,j} = t_{i,j} - t_{i-1,j}, i > 1$). Since the conditional density function (cdf) describing this Poisson inter-arrival time is shown in Section 2.2.4.1 to be an exponential process (2.9), and the expected value of an exponential process is the inverse of its rate parameter, Λ can be determined by finding the inverse of the MLE for the mean of an exponential random variable (3.9).

$$\Lambda = \frac{1}{\underline{\Delta t}} \quad (3.9)$$

3.2.2.3 γ

The first step in determining the large-scale parameter for intra-cluster decay time, γ , is to normalize each primary cluster per CIR and set the first arrival in each cluster to a time of zero. Since an exponential decay is observed, the amplitude should be in log-scale. Exponential functions are log-linear, so a linear regression fit is applied to the superimposition of all clusters to fit a line with MMSE to the intra-cluster decay. The determined slope, negated and converted back to linear-scale, is the intra-cluster decay time γ . A comparison between measured and modeled ray decay is shown in Figure 3.12.

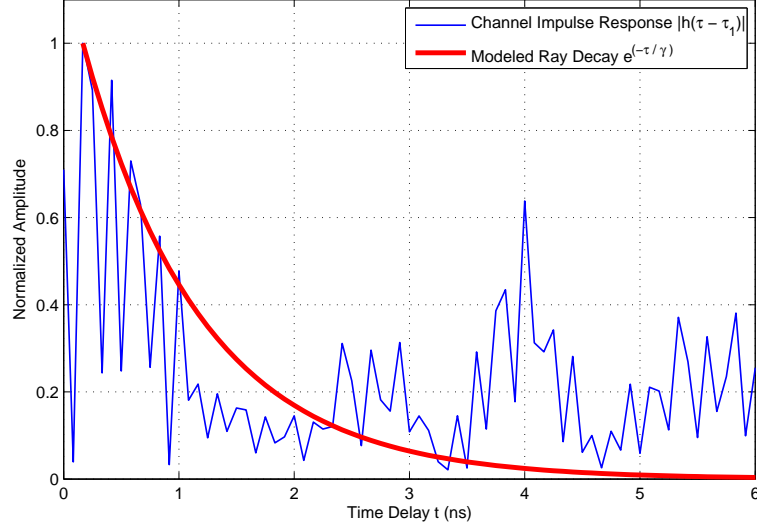


Figure 3.12: Channel ray decay measurement versus model.

3.2.2.4 $\Gamma, \sigma_{\text{cluster}}$

The large-scale parameters for inter-cluster decay time and cluster shadowing deviation, Γ and σ_{cluster} , are determined by applying a method similar to the CLEAN algorithm [37]. After normalizing each CIR, note the amplitude of the first cluster. Now, using the cluster arrival times and ray decay time calculated above, subtract the estimated time-domain energy profile of the first incident cluster. The amplitude of the second cluster can now be noted without the remaining energy of the first cluster. Remove the energy of the second cluster similarly and note the third cluster's peak amplitude. Repeat this process for all clusters until you have a matrix (3.10), where t_i, A_i , and n are the arrival time of the i th cluster, the absolute peak amplitude of this cluster, and the total number of clusters per CIR,

respectively.

$$\tilde{C} = \begin{bmatrix} A_1 & A_2 & \cdots & A_n \\ t_1 & t_2 & \cdots & t_n \end{bmatrix} \quad (3.10)$$

Superimpose the matrix of each cluster and compute a log-linear regression as above to determine Γ . A comparison between measured cluster decay and modeled cluster decay is shown in Figure 3.13. To find σ_{cluster} , consider the time-shifted

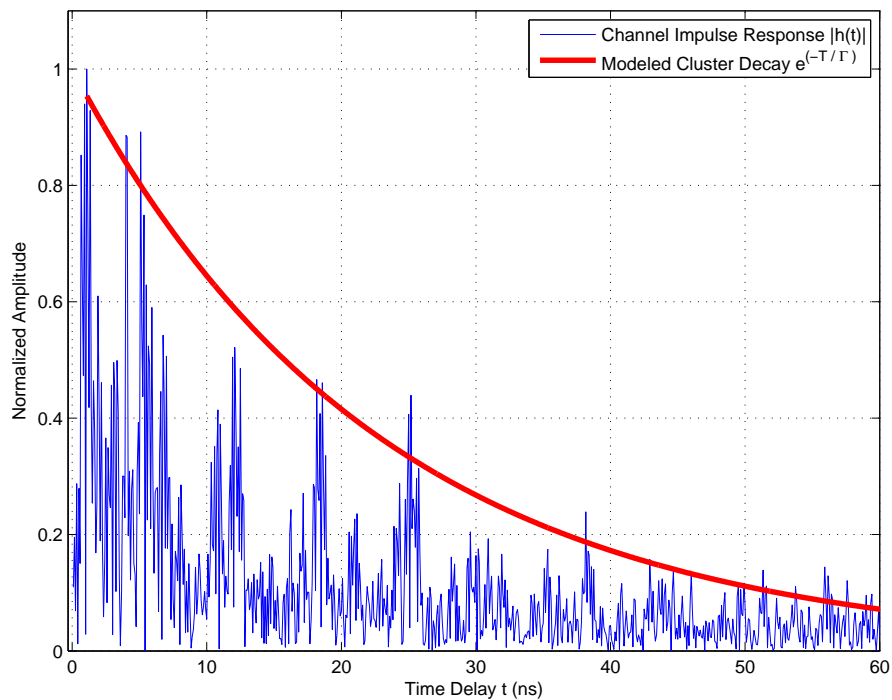


Figure 3.13: Channel cluster decay measurement versus model.

exponentially decreasing function $e^{-\tau/\Gamma}$ to be the mean function for matrix \tilde{C} and calculate the second central moment. The output value is σ_{cluster} .

3.2.2.5 μ_m, σ_m

Differences among CIRs corresponding to the same radial line segments are due to the small-scale fading within the channel. To extract the characteristic Nakagami m -factors, start by separating each CIR along a certain radial line into a series of resolvable delay bins, i.e. $\{0-5, 5-10, 10-15, \dots\}$ ns. For this thesis a bin size of 5 ns was chosen. Within each bin, k , of each radial arc location, i , are an equal number of energy values, $\{G_k^{(i)}\}$. The number of values depends on the size of the bin and the time-domain resolution of the CIR. From here, consider each arc individually. Each bin's energy values, $\{G_k\}$, must be fit to a distribution with descriptive parameters m_k and Ω_k . The distribution parameters for each bin k are calculated as shown in (3.11) and (3.12).

$$m_k = \frac{E^2[(G_k^{(i)})^2]}{\text{Var}[(G_k^{(i)})^2]} \quad (3.11)$$

$$\Omega_k = E[(G_k^{(i)})^2] \quad (3.12)$$

Construct a cdf using these parameters on a selection of bins and compare them to the measured cdf's to demonstrate the correctness of the extracted parameters as in Fig 3.14. The m parameters are a lognormally distributed random variable [18] and can therefore be fully described by mean and standard deviation. Use the equations for the mean and standard deviation of a lognormally distributed variate, (3.13) and (3.14) respectively, to calculate the final values μ_m and σ_m . It should be noted that, while m_k does vary based on its delay τ_k , the standard UWB channel

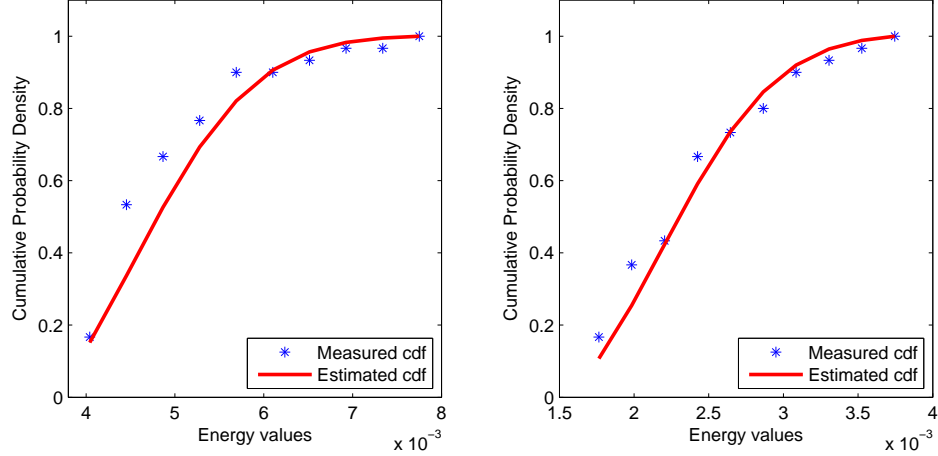


Figure 3.14: Measurement-derived cdf versus modeled cdf for two random bins.

model does not include this factor.

$$\mu_m = \ln(E[m_k]) - \frac{1}{2} \ln\left(1 + \frac{\text{Var}[m_k]}{E^2[m_k]}\right) \quad (3.13)$$

$$\sigma_m = \sqrt{\ln\left(1 + \frac{\text{Var}[m_k]}{E^2[m_k]}\right)} \quad (3.14)$$

3.2.2.6 $E\{\tau_{rms}\}$

The rms delay spread τ_{rms} of each CIR can be found from the second moment of the modified PDP. First, generate a modified PDP with only peak values. Align all peak values, a_k , with their respective delays, τ_k , and store these values in an array. Finally, use the equation shown in (2.13) to calculate the rms delay spread τ_{rms} for each PDP. Since this parameter is only used for gauging transmission

characteristics, the mean of these values, $E\{\tau_{rms}\}$, is sufficient information for this channel model.

3.2.3 Model parameters and comparison

Table 3.2 shows the CIR parameters extracted by the instructions above for the channel of interest. Note that, again, variables are divided into near-field and far-field scenarios. Dissimilarities between the model in this thesis and those already

Table 3.2: Channel Model Impulse Response Parameters.

Parameter	Near-field	Far-field
Valid Range (cm)	1 to d_{02}	d_{02} to 40
\bar{L}	18.27	29.71
Λ (1/ns)	0.377	0.376
Γ (ns)	17.13	23.03
γ (ns)	1.12	1.03
$\sigma_{cluster}$ (dB)	5.55	3.87
μ_m (dB)	1.57	1.76
σ_m (dB)	1.04	0.99
$E\{\tau_{rms}\}$ (ns)	25.65	23.62

in existence [2, 13–19] can be observed from Table 3.2. The most striking difference is the large mean number of clusters \bar{L} . Other models tend to have a value less than 10, whereas this model has double that amount in the near-field and triple that in the far-field regions. Note, however, that the inter-arrival rate Λ is also more than ten times that found in other UWB channel models. These are both excellent descriptors of the uncommonly large amount of multipaths that exist in the channel of interest. As previously stated, the fact that the channel is completely

shrouded in EM-reflective material causes the number of multipath clusters \bar{L} to skyrocket. Indeed, as is observable in Figure 3.13, it is sometimes difficult to distinguish individual multipath clusters (MPCs). The small size of the channel causes these MPCs to arrive in quick succession, shrinking the inter-arrival time and increasing Λ . The fairly high power of the MPCs will, however, allow for better SNR in non-line-of-sight (NLOS) conditions.

4 – Pulse Response

The channel model presented in Chapter 3 is a valid way to represent the communications channel of interest irrespective of the chosen radiation system. However, any physical UWB system implemented in this channel will have additional characteristics that must be observed to fully understand its functionality. First, it has been shown that there is a strong correlation between beamwidth and rms delay spread for directional antennas [47]. Second, it has been proven that no real UWB antenna provides true omnidirectional performance [48]. The manufacturer-determined radiation pattern for one professed omnidirectional UWB antenna is shown in Figure 4.1 [3]. It can be readily observed that this antenna, while omnidirectional in the azimuth cut ($\theta = 90^\circ$), is directional in the elevation cuts ($\phi = 0^\circ, \phi = 90^\circ$). Additionally, in [49] it is demonstrated that the UWB antenna chosen for a system will greatly affect the characteristics of the transmitted pulse. The UWB pulse width and shape varies with the relative angle between transmitter and receiver. Finally, interference generated within the channel can mask or hide the information signal. Since the channel of interest is unique in its path loss characteristics, and pulse shape and interference are important in any communications environment, understanding the effects of the chosen radiation system on a transmitted pulse in this particular case is vital to having a full understanding of the channel. Thus it is useful to implement a prototype system within the channel

of interest to characterize the expected signal alterations due to influences other than the physical channel.

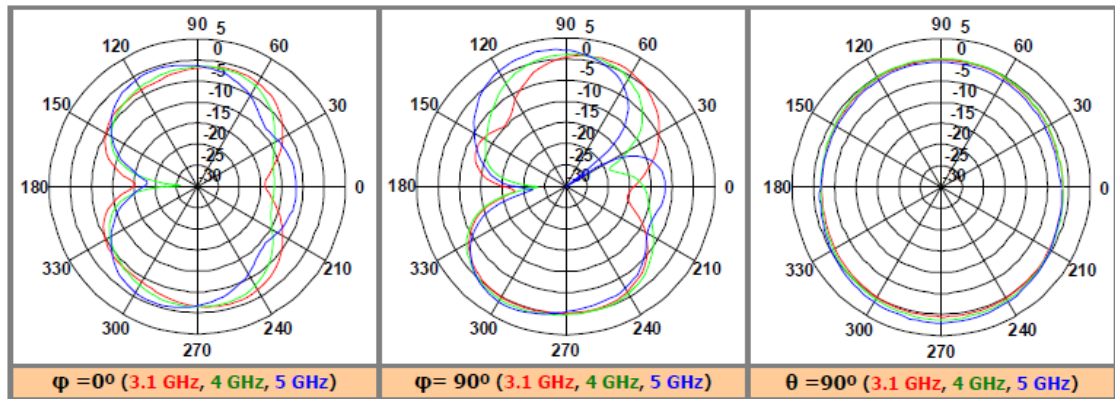


Figure 4.1: Radiation pattern of professed omnidirectional UWB antenna (from [3]).

While the end system described in Section 1.1 will exist within the integrated circuits (IC) designed for a computer, resources and time available at the time of this thesis were limited. IC design is a process which, for prototyping and proof-of-concept, is cost-prohibitive and time-consuming. Therefore to most accurately mimic the characteristics of the end system, a printed circuit board (PCB) implementation of a UWB pulser and receiver are designed and placed in the channel of interest to observe its UWB pulse response, the output of a system when the input is a pulse meeting FCC UWB requirements. The antenna used for the following measurements is a Fractus Media+ UWB Chip Antenna (FR05-S1-P-0-107) [3].

4.1 UWB Pulser

Observing the rms delay spread of the channel from Section 3.2.3, a maximum pulse repetition frequency (PRF) to prevent ISI (4.1) is approximately 38 MHz. A safe PRF of 10 MHz is chosen for the design of this pulser. Additionally, the FCC UWB mask from Figure 1.1 must be considered during the design process.

$$\text{PRF} \leq \frac{1}{\tau_{\text{rms}}} \quad (4.1)$$

4.1.1 Schematic design

The generation of UWB impulses is generally accomplished using one standard methodology. A very short pulse, on the order of 0.5 - 1 ns, is generated in a circuit using Step-Recovery Diodes (SRD). This pulse is then mixed with a carrier sinusoid somewhere in the 3.1 - 10.6 GHz range. The result is a brief high-frequency pulse like that in Figure 4.2 with a UWB frequency spectrum as shown in Figure 4.3. The generation of the short pulse can be accomplished by taking advantage of the avalanche characteristics of an SRD. SRDs act as charge-controlled switches in that, when forward-biased, they will accumulate charge until a reverse bias is applied. Once this occurs, the diode appears to have a very low impedance until the stored charge is depleted. Then the diode rapidly switches to a high-impedance state, blocking the reverse current of the SRD. By storing charge and switching impedance states very quickly, the SRD can be used to obtain extremely short bursts of energy, perfect for the generation of UWB baseband pulses [50]. The

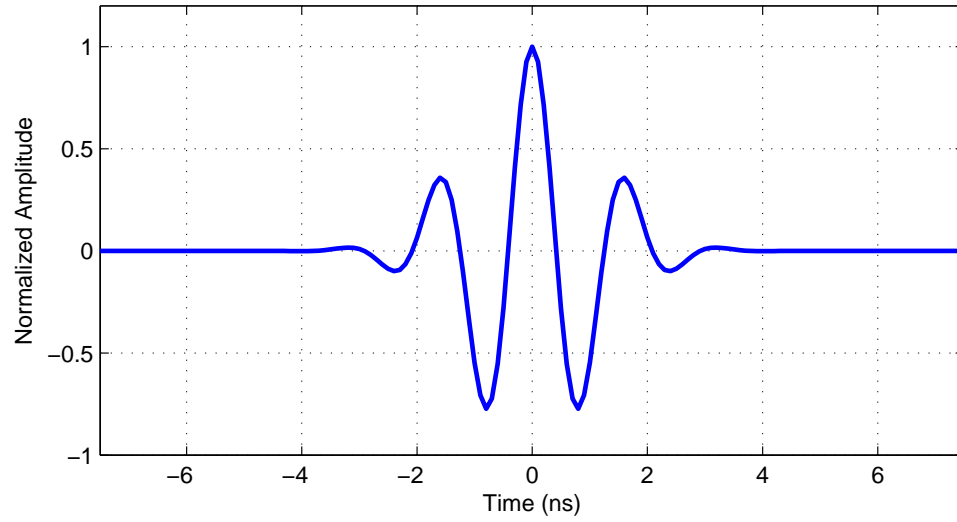


Figure 4.2: Ideal UWB pulse.

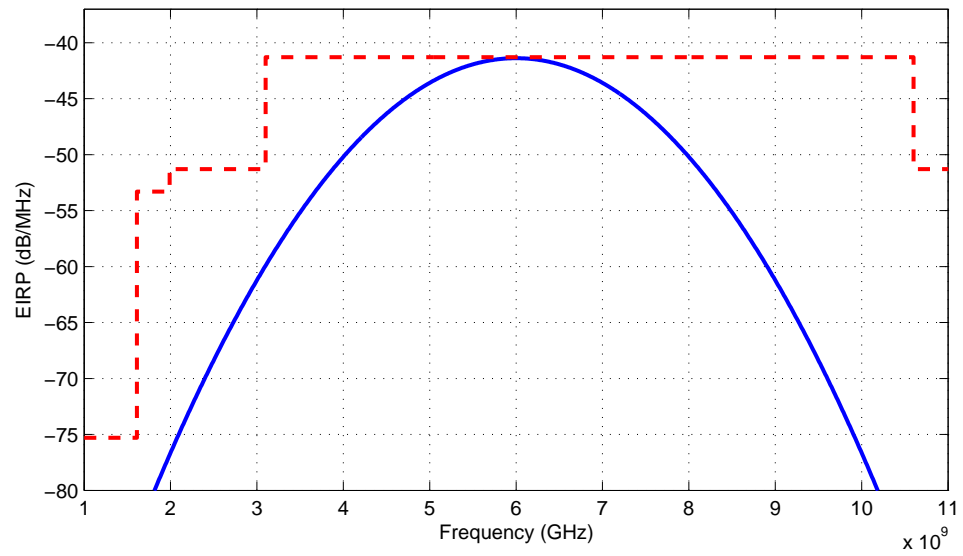


Figure 4.3: Frequency spectrum of ideal UWB pulse versus FCC spectral mask.

time to discharge the stored charge is proportional to the junction capacitance C_j , the time to switch to a high-impedance state is called the transition time t_s , and the time before the process can be repeated is the carrier lifetime t_l . C_j , t_s , and t_l are generally on the order of 0.2-2.0 pF, 50-200 ps, and 10-20 ns respectively, allowing pulse width generation in the hundreds of picoseconds and a maximum PRF of 50-100 MHz. Both of these estimates fit very well with the needs of an UWB pulser. A 10 MHz UWB pulse repeater can therefore be designed by keeping an SRD forward-biased and using a 10 MHz clock oscillator to repeatedly reverse-bias it, causing an energy discharge with duration proportional to a series capacitance as in Figure 4.4. Using this method, a strong positive pulse is generated on the rising-edge of the clock, and a negative pulse is generated on the falling-edge of the clock. To eliminate the negative pulse, a series Schottky diode is added after the pulse-shaping capacitor. The reverse-bias for the SRD is accomplished using a negative-voltage regulator and appropriately sized resistor. With this baseband pulse, the next step is to boost it to a carrier frequency so that the spectral mask will be met. This is normally accomplished by mixing the baseband pulse with a carrier sinusoid, however upon testing this circuit it was found that the oscillator leaked through the PCB dielectric FR4 and corrupted the output signal. An alternative method was therefore devised. First it should be noted that a sub-nanosecond pulse has spectral components up to 7-8 GHz, although they are of significantly diminished power. It follows that a well-shaped carrier-frequency UWB pulse can be generated passing a sub-nanosecond pulse through a UWB band-pass filter, such as a Taiyo Yuden FI212B396001-T filter [51] with 3.1-4.9

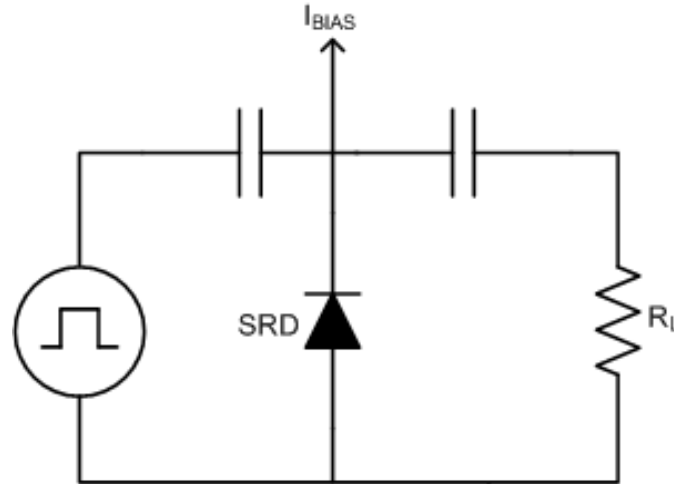


Figure 4.4: Basic nanosecond pulse generator.

GHz passband. Figure 4.5 shows a measured subnanosecond pulse and its band-pass filtered (BPF) counterpart. The frequency spectrum of this pulse is presented in Figure 4.6. The last step is to amplify the UWB pulse such that it is as large as possible but remains under the FCC spectral mask. The downside of using a BPF-generated pulse is that the output magnitude is very small, so more amplification is required. Two MiniCircuits MNA-7+ Power Amplifiers are used to boost the signal to an appropriate level. The schematic is split between the baseband pulse generator and the BPF to keep leakage from affecting the pulse shape. This is further discussed in Section 4.1.2. The schematics for the baseband and passband components of the UWB Pulser are shown in Figures 4.7 and 4.8. Note that the clock oscillator is on the passband board due to size constraints. The baseband pulse is passed through J2 on the baseband board to J3 on the passband board, and power is fed from J2 on the passband board to J1 on the baseband board. At

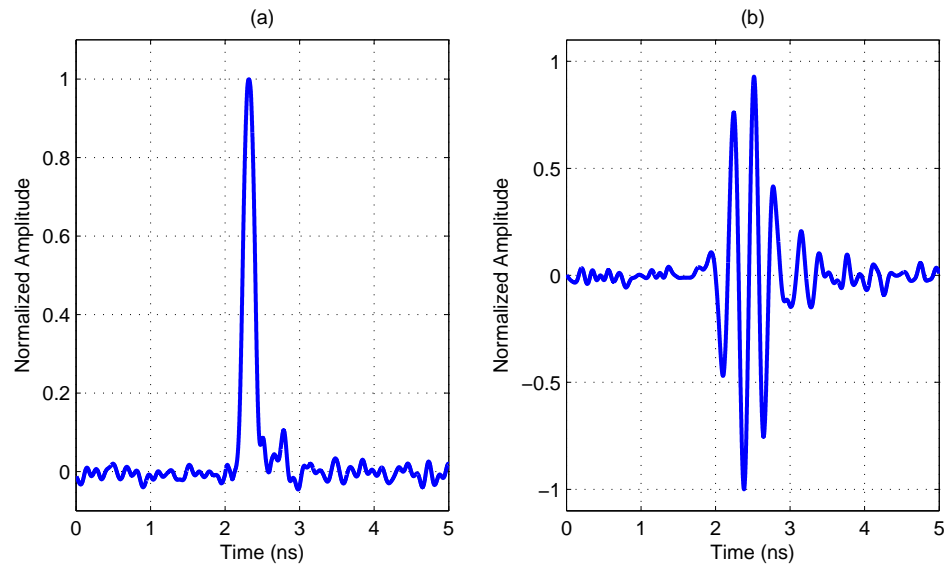


Figure 4.5: Equipment-generated subnanosecond pulse and BPF'd counterpart.

the time of development, a two-antenna system was needed, hence on the passband board the amplified pulse is passed through a splitter and there are two output ports J4 and J5.

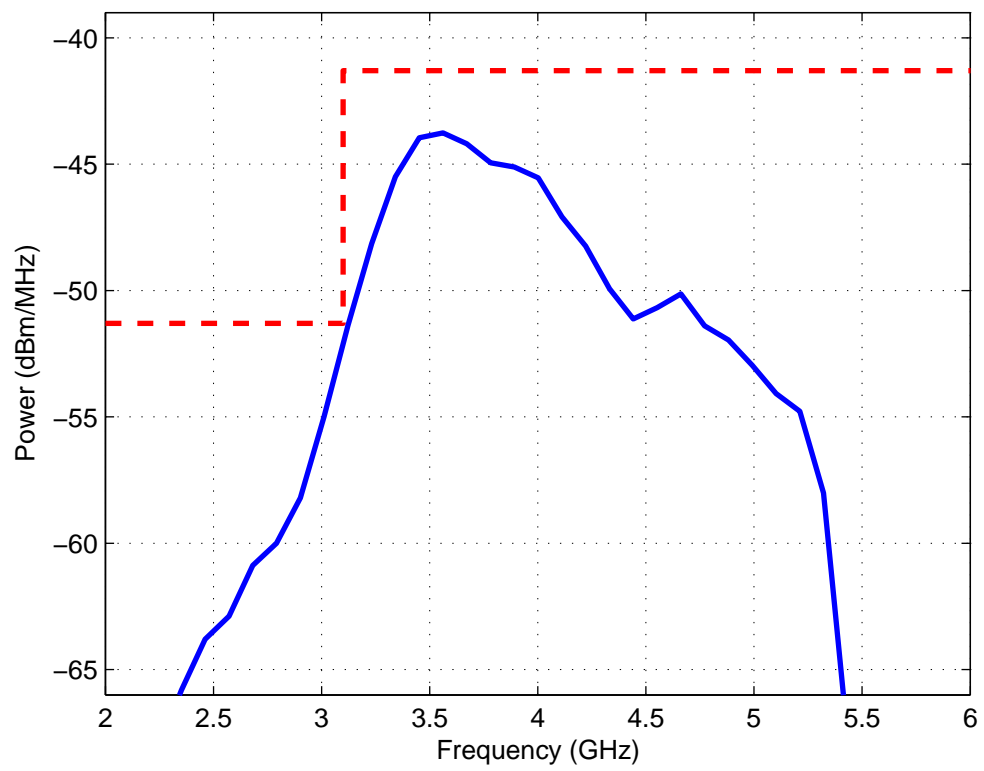


Figure 4.6: Frequency spectrum of BPF'd equipment-generated UWB impulse.

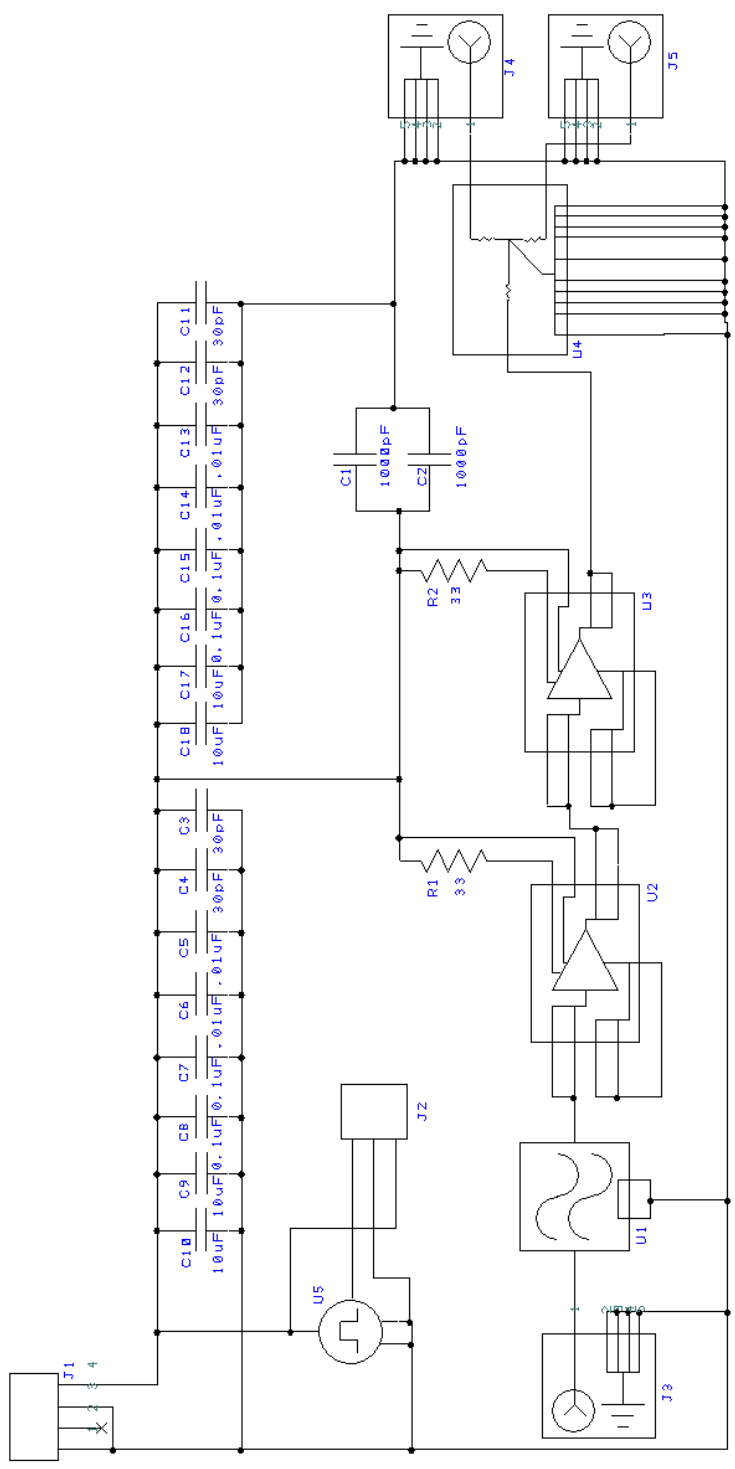


Figure 4.8: UWB pulser passband generator schematic.

4.1.2 Printed circuit board design

Before starting the PCB layout for the UWB pulser schematics in Figures 4.7 and 4.8, there are several important RF PCB design techniques to consider. First and foremost is the decision of how many board layers to use. The majority of simple low-frequency PCBs use a two-layered board because it is simpler and cheaper than those with more layers. Four-layer designs can provide better EM-shielding and power distribution, as well as giving more space for routing signal traces. With a four-layer board you can devote two layers to ground and one each to power and signal. The ground plane, an entire layer of the board devoted to ground, is a fundamental concept in RF circuit design. This plane allows all signals on the board to see it as an infinite ground and provides short current return paths to signal traces, mitigating noise, stray inductance, and signal oscillation [52]. The UWB pulser does not have any digital components, so the ground plane can cover the entire PCB layer.

The next design consideration is board stack-up. This includes which layers are assigned to ground, power, and signal, the separation between layers, and layer thickness. According to [53], the best stackup for EM-shielding is shown in Figure 4.9. The layer thickness and spacing are dependent on overall board thickness, and are important for determining controlled-impedance line widths. Choices in this area are usually limited by board vendor and cost. Signal lines which will carry high-frequency signals should have controlled impedance because maximum power is transferred when a component's source impedance, Z_s , is conjugate-equal



Figure 4.9: Recommended 4-layer board stackup for maximum EM-shielding.

to its load impedance, Z_l . Any mismatch between these two quantities causes part of the signal to be reflected back from the load along the line of transmission. This is vitally important not only to maximize the output signal's power, but also because reflections badly distort vital signals. Depending on the characteristics of the signal and the degree of reflection, signals can be altered to the point of meaninglessness, requiring complete board re-design. Generally speaking, controlled-impedance lines are only necessary when the line length is a large fraction of its signals shortest wavelength. For this design, the highest frequency is expected to be less than 6 GHz, so controlled impedance is necessary for line lengths $l > 1cm$. To calculate the line impedance for a stripline trace as in Figure 4.10 use (4.2) where ϵ_r depends on the dielectric material used in the board stackup [52]. Also make sure there are no 90° bends in transmission lines as these too can cause reflections.

$$Z_0(\Omega) = \frac{60}{\epsilon_r} \ln \left[\frac{1.9B}{0.8W + T} \right] \quad (4.2)$$

Another useful technique when designing an RF PCB is called stitching. The two types of stitching are trace stitching and board-edge stitching. This technique

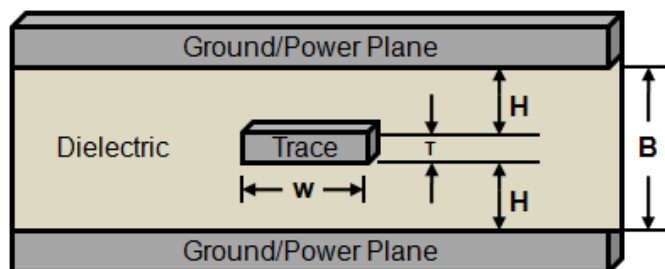


Figure 4.10: Stripline controlled-impedance line.

involves inserting numerous tightly spaced through-hole vias connecting the two ground planes along the sides of high-frequency traces and the edges of the ground planes. These stitches act similarly to a Faraday cage in that they diminish EM radiation with wavelengths significantly larger than the gaps between stitches. Examples of both types of stitching are shown in Figure 4.11. Finally, it is vitally

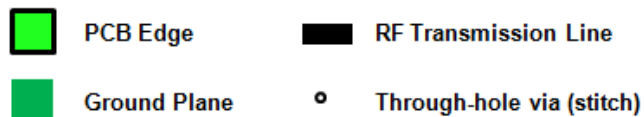
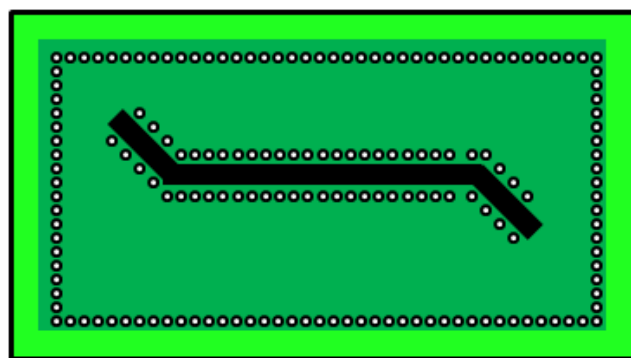


Figure 4.11: Board-edge and trace-lining stitching.

important to use decoupling capacitors near noisy circuit components to prevent the noise from leaking into signal lines. The PCB for the UWB pulser is designed

with all these considerations. The board stackup is as shown in Figure 4.9, with controlled-impedance trace widths of 0.015". These traces are kept as short as possible and sharp corners are avoided. Stitching is implemented along the edges of the ground planes and alongside signal traces. PCB layouts for the UWB Pulser baseband and passband boards are shown in Figures 4.12 and 4.13, respectively, excluding ground and power planes. The output signal from this pulser is shown in Figure 4.14.

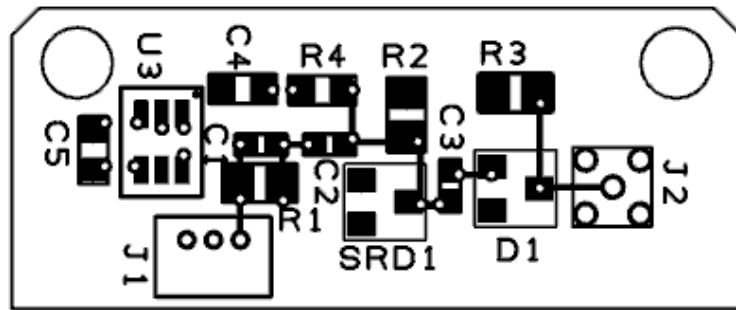


Figure 4.12: UWB pulser baseband generator PCB layout.

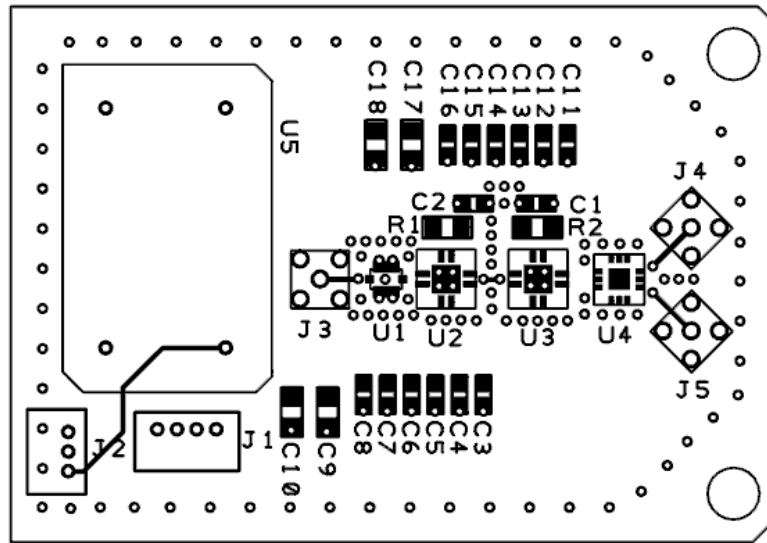


Figure 4.13: UWB pulser baseband generator PCB layout.

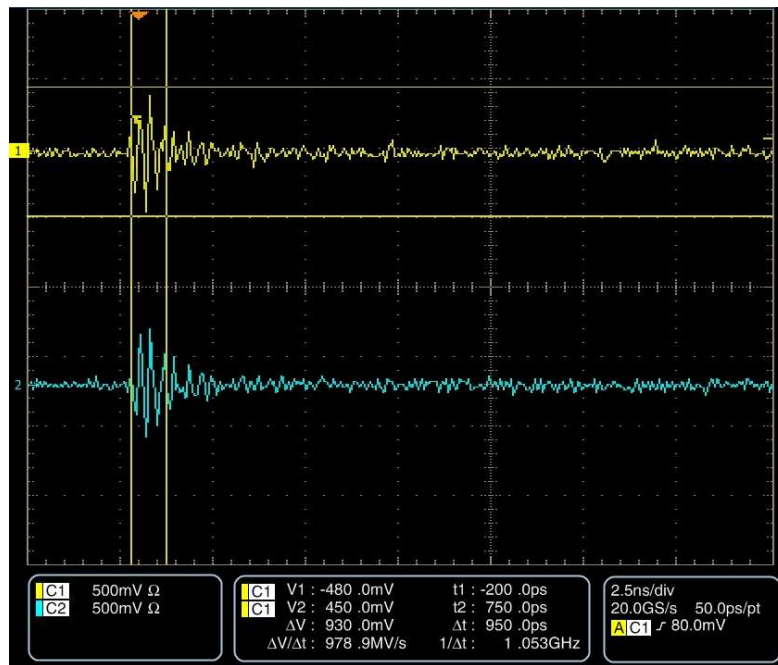


Figure 4.14: UWB pulser output pulse.

4.2 UWB Receiver

Because the expected input signal to this receiver is a multipath-distorted UWB impulse with a carrier frequency of approximately 4 GHz and 2 GHz bandwidth, a sampling frequency of at least 10 Gbps would be necessary to retrieve the full extent of the information carried by the transmitted pulse. Due to the lack of available 10 Gbps Analog-to-Digital Converters (ADC), the signal must be modulated back to the baseband before it is sampled. Very brief impulses are not well suited to locking carrier frequencies via phase-locked loops (PLL) so a non-coherent receiver architecture is desired. Figure 4.15 shows the architecture used in this receiver.

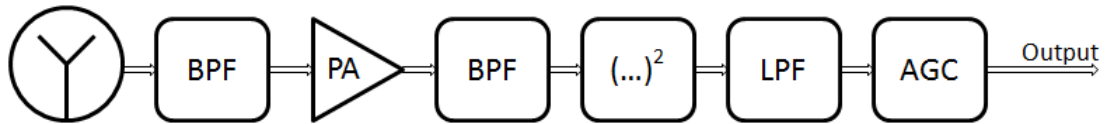


Figure 4.15: Typical non-coherent receiver.

Because it is prohibitively difficult to design an impulse peak-power detector on PCB, standard adjustable gain control (AGC) is not possible. Instead, an additional static-gain amplifier is added, followed by a variable attenuator (VA). This attenuator (Honeywell HRF-AT4610) can vary its level of attenuation between 0.5 and 31.5 dB rapidly enough to switch states between received impulses. Control for the VA is received from a field-programmable gate array (FPGA) fed by the system ADC, where an impulse peak-power detector will be implemented. Since the ADC and FPGA have not been implemented at the time of writing of this thesis, the VA will be set to 0.5dB to observe the output signal.

4.2.1 Schematic design

To determine the amount of gain desired from the power amplifier (PA) stage in Figure 4.15, the path loss model parameters from Table 3.1 is consulted. The maximum expected path loss at 45 cm, based on this information, will be approximately 30 dB. The amplifier selected for the design, Mini-circuits ERA-2SM+, has a gain of 12 dB at 5 GHz. There is some additional loss due to the insertion loss of the filtering stages and connectors. A conservative estimate for the number of amplifiers required to account for the system path loss is therefore four, generating a total gain of an estimated 40 dB.

Following convention, the design is split into two stages. Stage 1 consists of filtering and amplification elements restricted to passband operation. The initial design for Stage 1 includes π -type attenuators between amplifier stages for impedance matching, but it was determined through measurement that the circuit functions better without these attenuators. On the prototype board, these are bypassed using zero ohm resistors. Additionally, it was found that the BPFs of Stage 1 did not sufficiently attenuate frequencies below 3 GHz [51], causing a great deal of out-of-band noise. This was corrected by adding a high-pass filter (HPF) to the output of Stage 1. These changes are not reflected in the receiver schematics. The structure of the Stage 1 schematic, shown in Figure 4.16, is then a filter element, followed by four sequential amplifiers, followed by two filter elements.

Stage 2 consists of the square-law detector, followed by a low-pass filter (LPF) to eliminate high-frequency harmonics arising from the squaring operation, a pulse

amplifier, and a VA as described above. The original design used two LPFs of different cutoff frequencies, 1 GHz and 10 GHz, because the 1 GHz LPF had minimal attenuation above 9 GHz, but it was determined this was unnecessary, so the final implementation bypasses the second filter element. Schottky barrier diodes are used to implement the square-law detector [54]. The square-law detector circuit is limited in bandwidth dependent on the shunt capacitance placed after the diode and the characteristics of the diode itself. The relationship is shown in (4.3) from [55] where R_L is the load resistance, C_T is the shunt capacitance, and R_V is calculated from the parasitic elements of the diode.

$$f_{c(3dB)} = \frac{1}{2\pi R_T C_T} \text{ where } R_T = \frac{R_V R_L}{R_V + R_L} \quad (4.3)$$

The sensitivity of the square-law detector circuit can be increased by biasing the Schottky diode. The receiver was designed allowing for the implementation of biasing, but the associated components were not populated. Biasing the diode also has the effect of slightly increasing the cutoff frequency, but the effect is negligible for bandwidths greater than 100 MHz. The Stage 2 receiver schematic is shown in Figure 4.17.

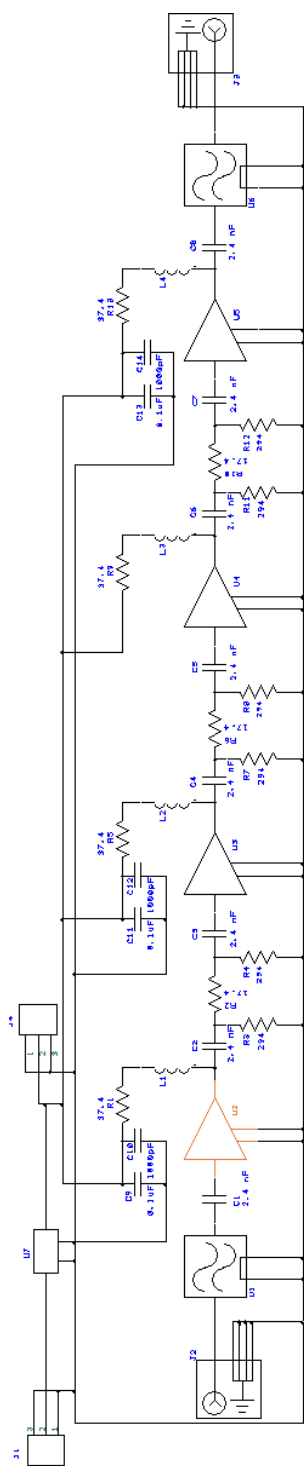


Figure 4.16: UWB receiver stage 1 schematic.

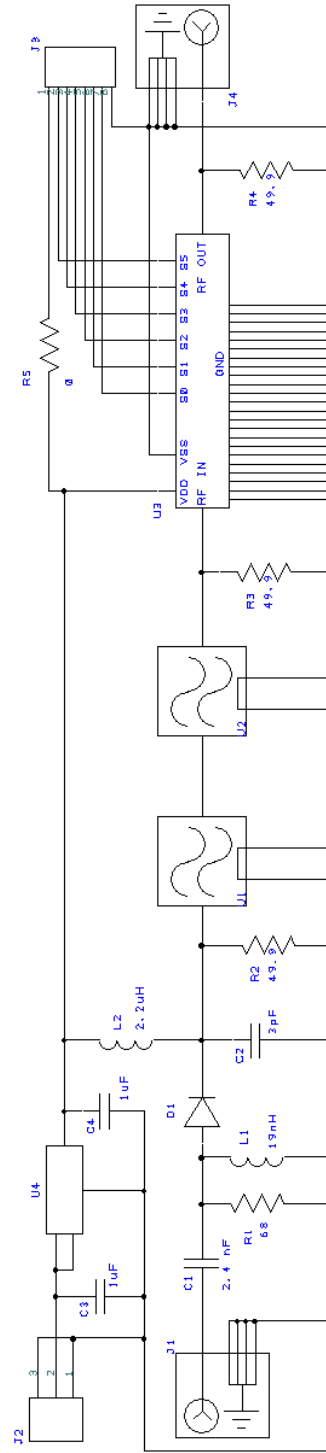


Figure 4.17: UWB receiver stage 2 schematic.

4.2.2 Printed circuit board design

The hardware design considerations for the UWB receiver PCB are the same as for the pulser. See Section 4.1.2 for details. PCB layouts for the UWB Receiver Stage 1 and Stage 2 boards are shown in Figures 4.18 and 4.19, respectively, excluding ground and power planes. The measured output signal from this receiver stimulated by a near-ideal input (Figure 4.5) is shown in Figure 4.20.

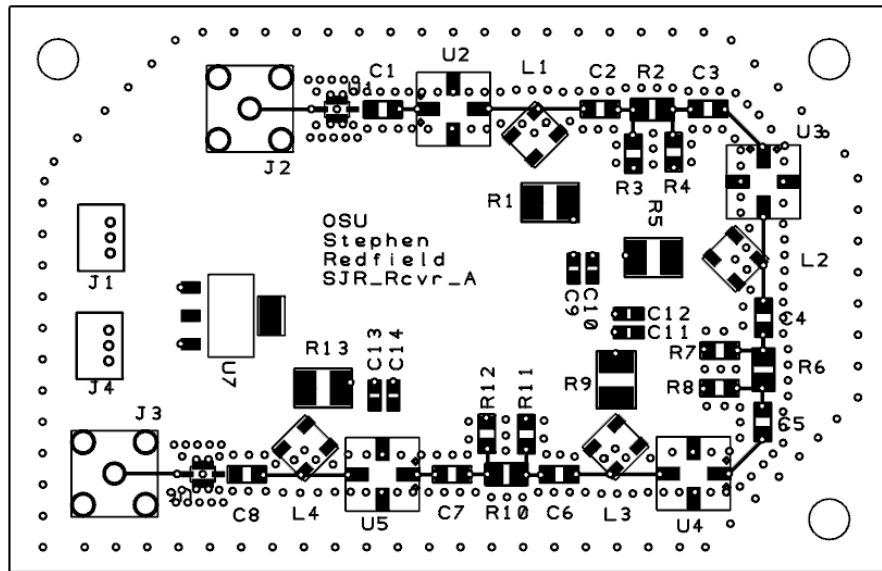


Figure 4.18: UWB receiver stage 1 PCB layout.

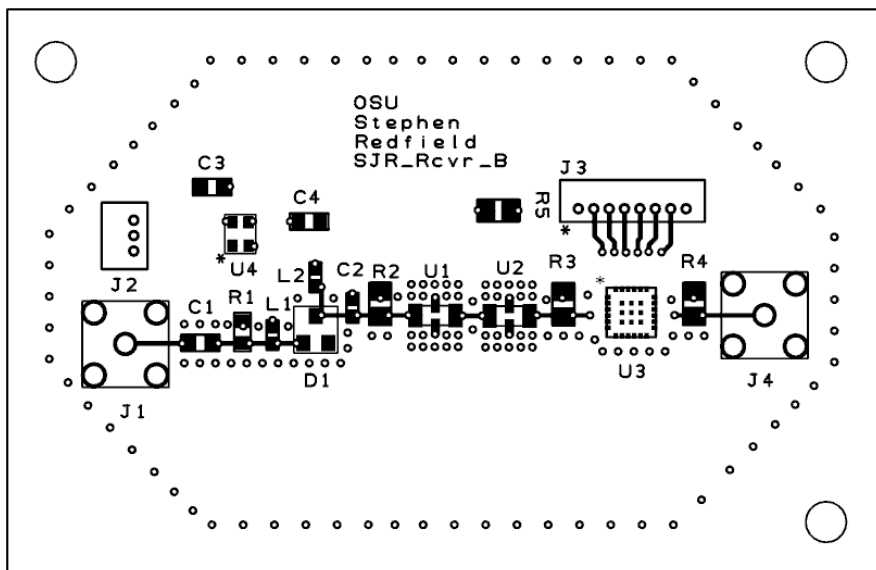


Figure 4.19: UWB receiver stage 2 PCB layout.

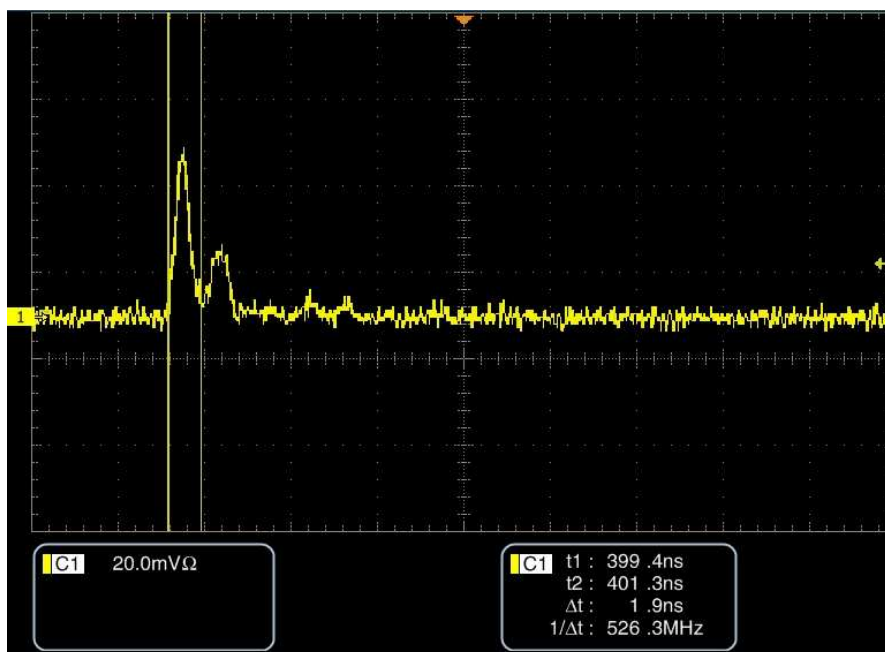


Figure 4.20: Receiver output with near-ideal input.

4.3 Results

The pulse response is characterized by experiment, where the pulser and receiver designed in Sections 4.1 and 4.2 were placed in the channel of interest. The computer comprising the channel of interest was turned off for the first series of measurements to observe the channel in a dormant state. The second series of measurements were taken with the computer and all its resources turned on, and thus interference generated from the digital and analog components of the computer motherboard will affect the pulse response. This experiment most closely mimics the final system implementation. A comparison of the two sets of measurements can be seen in Figure 4.21.

The first notable trait of this figure is that the two plots are nearly identical. From this it can be intuited that the noise interference generated by the fully operating PC is virtually eliminated by the filtering mechanisms of the receiver. It can also be noted upon comparing Figures 3.13 and 4.21 that the signal multipaths terminate far faster in the system response than in the channel impulse response. This matches well with the data presented in [56], demonstrating the correlation between the delay spread of a wireless system and the beam width of the application's antennas. Since UWB antennas cannot act as true omnidirectional antennas, the delay spread of any practical UWB system will be shorter than that presented in a model which neglects antenna effects, as in the standard method. The adjusted maximum PRF with zero ISI for this channel is therefore approximately 45 MHz.

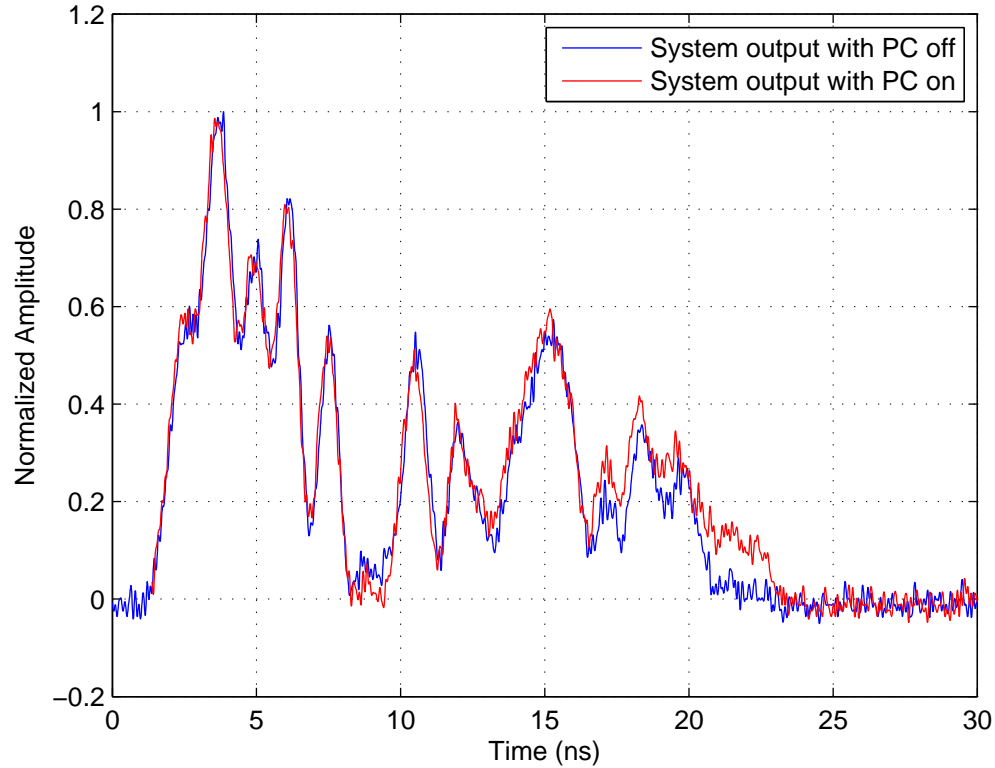


Figure 4.21: Comparison of complete system outputs with computer turned off and on.

Another difference from the presented channel model is the number of clusters. By visual inspection, there appear to be three primary clusters present. The logical reason for this dramatically different number is the difference in bandwidth between the ideal impulse used to generate the model in Table 3.2 and the non-ideal pulse generated to observe the pulse response. Since the bandwidth is dramatically less, the time-domain resolution of clusters is also reduced, diminishing the ability to pick out individual clusters. Additionally, there is distortion from the

expected pulse shape as shown in Figure 4.20, but this is slight enough as to not impede communications. It is therefore apparent that the most dominant obstacle to communications within this channel is the extremely dense multipath.

4.4 Future Development

Contingent on future time and funding constraints, the development of the system for replacing wired interconnects with broadcast wireless will continue primarily in the form of the development of embedded UWB transceivers. The UWB pulse and receiver presented above must be re-designed so as to be included in the design of computer ICs, and contain a process for the conversion of JTAG signals into a control sequence for data pulses. Because of the dense multipath and long delay spread demonstrated in Chapter 3, transceiver structures will also require methods such as transmitter equalization [57] or pre-rake algorithms [58] to increase the data rate above 45 Mbps while maintaining reasonable bit-error-rates.

It has also been suggested that a 60 GHz communications system would be appropriate for the change from wired interconnects to wireless. An effort therefore must be made to understand the channel of interest for this frequency band. This has not been undertaken specifically due to equipment limitations, and when such equipment becomes available, a campaign will follow, to model the channel of interest for 60 GHz omnidirectional communications.

5 – Conclusion

A brief introduction and motivation for wireless interconnects in PC systems has been given. The standard UWB channel model has been explained, and the steps to derive such a model have been given in detail. Subsequent to reading this thesis, one will be able to derive their own UWB channel model for multipath channels. The model specific to the environment within a PC chassis has been experimentally derived through a comprehensive measurement campaign and delivered with explanations of parameters. A UWB pulser and receiver have been designed for wireless interconnects proof-of-concept within the channel of interest. The pulse response of the channel, accounting for the effects of ambient noise radiation and transmission devices, has been observed. This has been used to approximate a baseline PRF of 45 Mbps for ISI-free communications within the channel and to determine whether or not environmental or antenna-generated distortion will negatively impact the desired communications systems. Finally, future development for communications systems in the channel of interest have been briefly discussed.

Bibliography

- [1] I. Oppermann, M. Hamalainen, and J. Iianatti, *UWB: Theory and Applications*. Chichester, West Sussex, England: John Wiley & Sons, 2004.
- [2] D. Cassioli, M. Win, and A. Molisch, "The ultra-wide bandwidth indoor channel: from statistical model to simulations," *IEEE Journal on Selected Areas in Communications*, vol. 20, no. 6, pp. 1247–1257, Aug. 2002.
- [3] Fractus. (2008, Apr.) Fractus Media+ UWB chip antenna datasheet. [Online]. Available: http://www.fractus.com/sales_documents/FR05-S1-P-0-107/UM_FR05_S1_P_0_107.pdf
- [4] M. Win and R. Scholtz, "Impulse radio: how it works," *IEEE Communications Letters*, vol. 2, no. 2, pp. 36–38, Feb. 1998.
- [5] S. Gezici, Z. Tian, G. Giannakis, H. Kobayashi, A. Molisch, H. Poor, and Z. Sahinoglu, "Localization via ultra-wideband radios: a look at positioning aspects for future sensor networks," *IEEE Signal Processing Magazine*, vol. 22, no. 4, pp. 70–84, Jul. 2005.
- [6] R. Qiu, H. Liu, and X. Shen, "Ultra-wideband for multiple access communications," *IEEE Communications Magazine*, vol. 43, no. 2, pp. 80–87, Feb. 2005.
- [7] M. diBenedetto, T. Kaiser, A. Molisch, I. Oppermann, C. Politano, and D. E. Porcino, *UWB Communications Systems: A Comprehensive Overview*. Hindawi: EURASIP, 2005.
- [8] "IEEE Standard Test Access Port and Boundary-Scan Architecture," *IEEE Std 1149.1-2001*, pp. 1–200, 2001.
- [9] B. Eklow, "Boundary-scan: Built to last? panel synopsis," in *IEEE International Test Conference*, Oct. 2007, pp. 1–1.
- [10] H. Eberle, A. Wander, and N. Gura, "Testing systems wirelessly," in *Proc. IEEE VLSI Test Symposium*, Apr. 2004, pp. 335–340.

- [11] S. Mekki, J.-L. Danger, B. Miscopain, and J. Boutros, "A simplified implementation of a probabilistic equalizer for impulse radio UWB in high data rate transmission," in *2nd International Conference on Signal Processing and Communication Systems*, Dec. 2008, pp. 1–7.
- [12] S. Galler, J. Schroeder, G. Rahmatollahi, K. Kyamakya, and K. Jobmann, "Analysis and practical comparison of wireless lan and ultra-wideband technologies for advanced localization," in *IEEE/ION Position, Location, And Navigation Symposium*, Apr. 2006, pp. 198–203.
- [13] R. Saadane, A. Hayar, H. Hofstetter, and D. Aboutajdine, "Statistical UWB channel model parameters estimation based on sage algorithm," in *Second International Conference on Communications and Networking in China*, Aug. 2007, pp. 1195–1199.
- [14] P. Richardson, W. Xiang, and W. Stark, "Modeling of ultra-wideband channels within vehicles," *IEEE Journal on Selected Areas in Communications*, vol. 24, no. 4, pp. 906–912, Apr. 2006.
- [15] C.-C. Chong, Y. Kim, and S.-S. Lee, "Statistical characterization of the UWB propagation channel in various types of high-rise apartments," in *IEEE Wireless Communications and Networking Conference*, vol. 2, Mar. 2005, pp. 944–949 Vol. 2.
- [16] C. Chong, Y. Kim, S. Yong, and S. Lee, "Statistical characterization of the UWB propagation channel in indoor residential environment," *Wireless Communications and Mobile Computing, Wiley InterScience*, vol. 5, no. 5, p. 503512, Aug. 2005.
- [17] J. Karedal, S. Wyne, P. Almers, F. Tufvesson, and A. Molisch, "A measurement-based statistical model for industrial ultra-wideband channels," *IEEE Transactions on Wireless Communications*, vol. 6, no. 8, pp. 3028–3037, Aug. 2007.
- [18] A. F. Molisch *et al.*, "IEEE 802.15.4a channel model-final report." IEEE, Tech. Rep. Doc. IEEE 802.15-04-0662-02-004a, 2005.
- [19] A. Molisch, D. Cassioli, C.-C. Chong, S. Emami, A. Fort, B. Kannan, J. Karedal, J. Kunisch, H. Schantz, K. Siwiak, and M. Win, "A comprehensive standardized model for ultrawideband propagation channels," *IEEE*

Transactions on Antennas and Propagation, vol. 54, no. 11, pp. 3151–3166, Nov. 2006.

- [20] H. Schantz, “Near field propagation law a novel fundamental limit to antenna gain versus size,” in *IEEE Antennas and Propagation Society International Symposium*, vol. 3A, Jul. 2005, pp. 237–240 vol. 3A.
- [21] S. Tanchotikul, P. Supanakoon, S. Promwong, and J.-i. Takada, “Statistical model rms delay spread in UWB ground reflection channel based on peak power loss,” in *International Symposium on Communications and Information Technologies*, Sep. 2006, pp. 619–622.
- [22] Q. Spencer, B. Jeffs, M. Jensen, and A. Swindlehurst, “Modeling the statistical time and angle of arrival characteristics of an indoor multipath channel,” *IEEE Journal on Selected Areas in Communications*, vol. 18, no. 3, pp. 347–360, Mar. 2000.
- [23] P. Smulders and L. Correia, “Characterisation of propagation in 60 ghz radio channels,” *Electronics Communication Engineering Journal*, vol. 9, no. 2, pp. 73–80, Apr. 1997.
- [24] H. Xu, V. Kukshya, and T. Rappaport, “Spatial and temporal characteristics of 60-ghz indoor channels,” *IEEE Journal on Selected Areas in Communications*, vol. 20, no. 3, pp. 620–630, Apr. 2002.
- [25] N. Moraitis and P. Constantinou, “Indoor channel measurements and characterization at 60 ghz for wireless local area network applications,” *IEEE Transactions on Antennas and Propagation*, vol. 52, no. 12, pp. 3180–3189, Dec. 2004.
- [26] C. Liu, E. Skafidas, and R. Evans, “Characterization of the 60 ghz wireless desktop channel,” *IEEE Transactions on Antennas and Propagation*, vol. 55, no. 7, pp. 2129–2133, Jul. 2007.
- [27] B. Qin, H. Chen, X. Wang, A. Wang, Y. Hao, L. Yang, and B. Zhao, “A single-chip 33pj/pulse 5th-derivative gaussian based IR-UWB transmitter in 0.13 μm CMOS,” in *IEEE International Symposium on Circuits and Systems*, May 2009, pp. 401–404.

- [28] S. Diao and Y. Zheng, "An ultra low power and high efficiency UWB transmitter for wpan applications," in *34th European Solid-State Circuits Conference*, Sep. 2008, pp. 334–337.
- [29] J. Zhang, S. Zhang, S. Wang, J. Qiu, and R. Zhou, "A fully integrated CMOS UWB transmitter," in *7th International Conference on ASIC*, Oct. 2007, pp. 372–374.
- [30] J. Lowe, H. Nie, and Z. Chen, "A code-shifted reference impulse radio ultra-wideband (IR-UWB) transmitter," in *IEEE Radio and Wireless Symposium*, Jan. 2010, pp. 535–538.
- [31] V. Kulkarni, M. Muqsith, K. Niitsu, H. Ishikuro, and T. Kuroda, "A 750 mb/s, 12 pj/b, 6-to-10 ghz CMOS IR-UWB transmitter with embedded on-chip antenna," *IEEE Journal of Solid-State Circuits*, vol. 44, no. 2, pp. 394–403, Feb. 2009.
- [32] Y. Zhao, Y. Dong, J. Gerrits, G. van Veenendaal, J. Long, and J. Farserotu, "A short range, low data rate, 7.2 ghz-7.7 ghz FM-UWB receiver front-end," *IEEE Journal of Solid-State Circuits*, vol. 44, no. 7, pp. 1872–1882, Jul. 2009.
- [33] N. Van Helleputte, M. Verhelst, W. Dehaene, and G. Gielen, "A reconfigurable, 130 nm CMOS 108 pj/pulse, fully integrated IR-UWB receiver for communication and precise ranging," *IEEE Journal of Solid-State Circuits*, vol. 45, no. 1, pp. 69–83, Jan. 2010.
- [34] A. Gerosa, S. Solda, A. Bevilacqua, D. Vogrig, and A. Neviani, "An energy-detector for noncoherent impulse-radio UWB receivers," *IEEE Transactions on Circuits and Systems I: Regular Papers*, vol. 56, no. 5, pp. 1030–1040, May 2009.
- [35] N. Beaulieu and B. Hu, "Soft-limiting receiver structures for time-hopping UWB in multiple-access interference," *IEEE Transactions on Vehicular Technology*, vol. 57, no. 2, pp. 810–818, Mar. 2008.
- [36] A. Saleh and R. Valenzuela, "A statistical model for indoor multipath propagation," *IEEE Journal on Selected Areas in Communications*, vol. 5, no. 2, pp. 128–137, Feb. 1987.

- [37] M. Peichl, M. Greiner, and H. Suess, "DLR activities on aperture synthesis radiometry," in *Proc. IEEE International Geoscience and Remote Sensing Symposium*, vol. 7, 2000, pp. 2981–2983.
- [38] R.-M. Cramer, R. Scholtz, and M. Win, "Evaluation of an ultra-wide-band propagation channel," *IEEE Transactions on Antennas and Propagation*, vol. 50, no. 5, pp. 561–570, May 2002.
- [39] B. Kannan *et al.*, "UWB channel characterization in outdoor environments," IEEE, Tech. Rep. Doc. IEEE 802.15-04-0440-00-004a, 2004.
- [40] B. Sklar, "Rayleigh fading channels in mobile digital communication systems .i. characterization," *IEEE Communications Magazine*, vol. 35, no. 7, pp. 90–100, Jul. 1997.
- [41] J. Aitchison and J. Brown, *The Lognormal Distribution, with Special Reference to its Use in Economics*. New York: Cambridge University Press, 1957.
- [42] D. Cox and R. Leck, "Correlation bandwidth and delay spread multipath propagation statistics for 910-MHz urban mobile radio channels," *IEEE Transactions on Communications*, vol. 23, no. 11, pp. 1271–1280, Nov. 1975.
- [43] J. Kunisch and J. Pamp, "Measurement results and modeling aspects for the UWB radio channel," in *IEEE Conference on Ultra Wideband Systems and Technologies*, 2002, pp. 19–23.
- [44] Skycross. (2009) Skycross SMT-3TO10M-A datasheet. [Online]. Available: <http://www.skycross.com/products/PDFs/SMT-3TO10M-A.pdf>
- [45] S. Ghassemzadeh, R. Jana, C. Rice, W. Turin, and V. Tarokh, "Measurement and modeling of an ultra-wide bandwidth indoor channel," *IEEE Transactions on Communications*, vol. 52, no. 10, pp. 1786–1796, Oct. 2004.
- [46] M. Win, R. Scholtz, and M. Barnes, "Ultra-wide bandwidth signal propagation for indoor wireless communications," in *IEEE International Conference on Communications*, vol. 1, Jun. 1997, pp. 56–60 vol.1.
- [47] C. Ho and T. Rappaport, "Effects of antenna polarization and beam pattern on multipath delay spread and path loss in indoor obstructed wireless channels," in *International Conference on Universal Personal Communications*, Oct. 1992, pp. 04.02/1–5.

- [48] Y. Takeuchi, Y. Shimizu, and Y. Sanada, "Experimental examination of antennas for a UWB positioning system," in *IEEE International Conference on Ultra-Wideband*, Sep. 2005, pp. 269–274.
- [49] R. Ye, S. Redfield, and H. Liu, "Technical challenges toward robust, high-precision ultra-wideband indoor localization," *unpublished*.
- [50] Hewlett-Packard, "Application note 918: Pulse and waveform generation with step recovery diodes," Oct. 1984.
- [51] T. Yuden. (2008) Taiyo Yuden FI212B396001-T datasheet. [Online]. Available: http://www.yuden.co.jp/us/product/pdf/ffi2_e.pdf
- [52] J. Ardizzoni, "A practical guide to high-speed printed-circuit-board layout," *Analogue Dialogue*, vol. 39, Sep. 2005.
- [53] H. Ott. (2007) Electromagnetic compatibility consulting and training: Tech tips. [Online]. Available: <http://www.test.org/doi/>
- [54] Hewlett-Packard, "Application note 986: Square law and linear detection," 1981.
- [55] ———, "Application note 923: Schottky barrier video detectors," 1999.
- [56] T. Taga and T. Tanaka, "Delay spread reduction effect of beam antenna and adaptively controlled beam facing access system in urban line-of-sight street microcells," *IEEE Transactions on Vehicular Technology*, vol. 52, no. 4, pp. 761–771, Jul. 2003.
- [57] C. Hu, S. Redfield, H. Liu, R. Khanna, J. Nejedlo, and P. Chiang, "Transmitter equalization for multipath interference cancellation in impulse radio ultra-wideband(IR-UWB) transceivers," in *International Symposium on VLSI Design, Automation and Test*, Apr. 2009, pp. 307–310.
- [58] K. Usuda, H. Zhang, and M. Nakagawa, "Pre-rake performance for pulse based UWB system in a standardized UWB short-range channel," in *IEEE Wireless Communications and Networking Conference*, vol. 2, Mar. 2004, pp. 920–925.

